CHALMERS

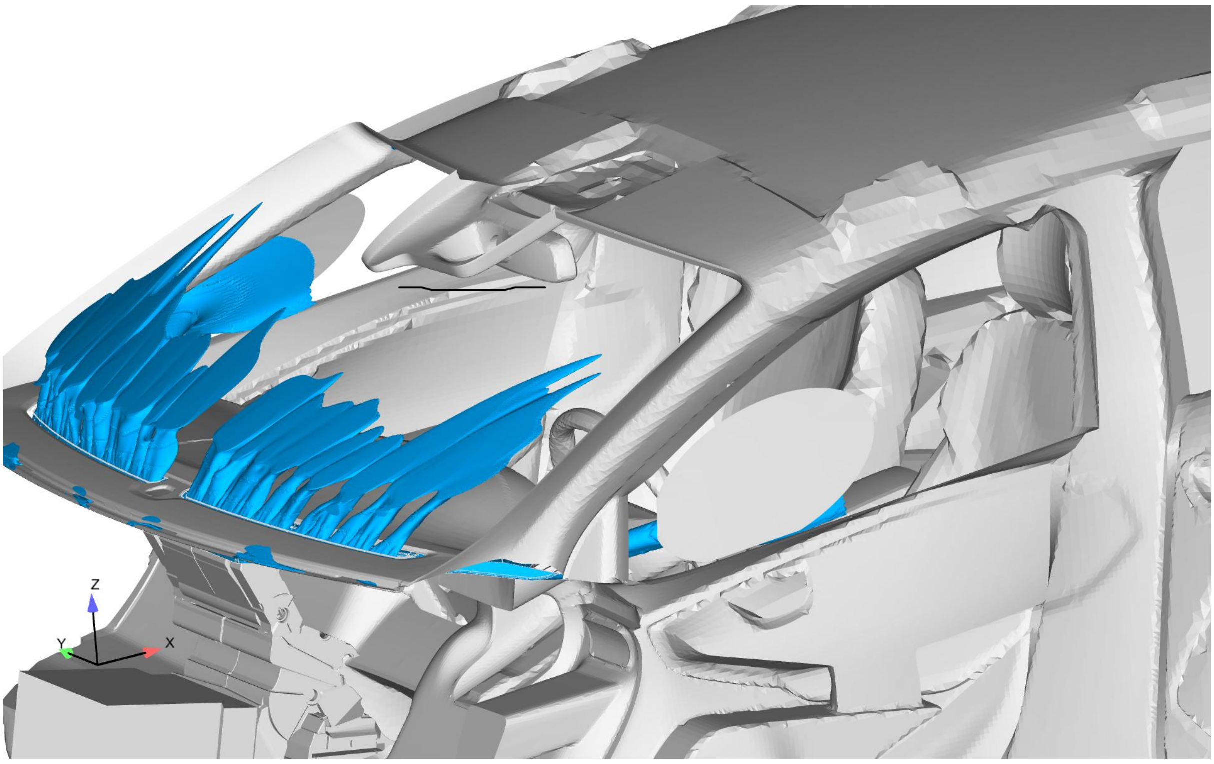

Improving the Accuracy of CFD Method for Windscreen Deicing

THEJESHWAR SADANANDA

Department of Applied Mechanics
Division of Fluid Dynamics
CHALMERS UNIVERSITY OF TECHNOLOGY
Göteborg, Sweden 2016

Acknowledgement

I would like to thank my supervisors Anders Björtin and Martin Hübert for giving an opportunity to pursue Master thesis at Volvo Cars. During the Master thesis, there was always a constant support which made me to execute the thesis to my fullest capabilities. Moreover my colleagues Frida Nordin, Mattias Wångblad and Michael Mackenzie from Climate CFD group assisted me whenever I needed them. I am also grateful to Kristina Sulz and Kristian Schmechtig for their kind support and co-operation to execute the deicing test in the best possible way. I would also like to thank other colleagues from Contamination & Core CFD group, Thermodynamics group and Aerodynamics group who made this tenure to be a pleasant and memorable one. Finally I would also like to thank my thesis examiner Professor Srdjan Sasic for giving enough freedom and support to explore possible ways to improve accuracy of CFD method for windscreen deicing.

Abstract

During winter, ice formed on the windscreen has to be removed before driving the vehicle. It is not safe to drive the vehicle without clear visibility on the windscreen. The defroster system in passenger cars melts ice on the windscreen. During the development of defroster systems, car manufacturers conduct physical tests to measure their performance. The performance of various design models are predicted through physical tests which consumes large amount of time. At Volvo Cars, Computational Fluid Dynamics(CFD) is used extensively to analyse the performance of various attributes of the car which reduces substantial amount of development time.

The objective of the master thesis is to improve the accuracy of the current CFD method in predicting the melting pattern of ice over the windscreen. The Volvo V40 model is used to analyse the performance of the defroster models. The Volvo V40 CAD model is surface meshed using ANSA meshing software which is then followed by generating the volume mesh using Harpoon meshing software. Boundary layers are generated at the cabin surface interface with the windscreen. In addition to it, three layers of windscreen and ice are modelled as prism layers using Fluentmesh to accurately predict the temperature and melting pattern at the external boundary of ice.

Steady state defroster flow is analysed to predict that the flow coming out from the defroster nozzles is uniformly distributed over the windscreen. The steady state flow simulation are carried out using $realizable\ k-\epsilon$ and $k-\omega\ SST$ turbulence model for modeling the turbulent flow in the defroster domain. It is found that the $realizable\ k-\epsilon$ turbulence model performed better than the $k-\omega\ SST$ turbulence model in solving the defroster flow field. Having known the distribution of the defroster flow, transient thermal analysis is performed by use of $Solidification\ and\ Melting$ model and modified various boundary conditions.

By varying the thermal properties of air from constant to a polynomial function of temperature and followed by modifying the boundary conditions of certain walls like A-pillar, instrument panel and front doors from adiabatic to temperature thermal boundary condition (using a transient temperature profile) there is some amount of improvement in the performance of the transient CFD model. However, consideration of radiation effect on certain walls did not have any influence in the transient simulation results. Moreover the selection of unsteady first order discretization scheme predicted the melting of ice quicker occur over the windscreen than unsteady second order scheme. The melting pattern obtained using unsteady first order scheme correlates better to the physical test results. Finally with the consideration of heat energy supplied across the heater instead of specifying the transient temperature profile at the inlet of HVAC unit, accuracy of the transient model improved significantly. It is believed that by taking into account source terms like gravitational force, buoyancy force in the solidification and melting model in addition to the implementation of sliding of partially melted ice occur over the windscreen can lead to further improvement in the performance of transient CFD models.

Nomenclature

Variables

ρ	Density	kg/m^3	σ	Turbulent Prandtl number	
u	Instantaneous velocity	m/s	G	Production term	kg/ms^3
p	Instantaneous pressure	N/m^2	ϵ	Dissipation rate	m^2/s^3
F	Body force	N	A$_{mush}$	Mushy Zone Constant	
ν	Kinematic viscosity	m^2/s	ω	Specific dissipation rate	1/s
$\overline{u}$	Time average velocity	m/s	μ_t	Tubulent dynamic viscosity	Ns/m^2
$u^{'}$	Fluctuating velocity	m/s	μ	Dynamic viscosity	Ns/m^2
$\overline{P}$	Time average pressure	N/m^2	H	Total enthalpy	J
$p^{'}$	Fluctuating pressure	N/m^2	λ	Under relaxation factor	
τ	Reynold's stress	N/m^2	L	Mean latent heat	J/kg
ν_t	Turbulent viscosity	m^2/s	Y	Dissipation	kg/ms^3
$\overline{u_i^{'}u_j^{'}}$	Time average Reynold's stress	m^2/s^2	E	Energy	J
k	Turbulent kinetic energy	m^2/s^2	k	Thermal conductivity	W/mk
δ	Kronecker delta		τ	Shear stress	N/m^2
h	Sensible enthalpy	J	T	Temperature	K
Y_j	Mass fraction	kg/mol	c_p	specific heat capacity	J/kgK
H	Latent heat	J	β	Coefficient of thermal expansion	1/K
β_L	Liquid fraction		S	Strain rate	1/s

Subscripts

i, j	Co-ordinate direction
t	Turbulent variable
k	Turbulent kinetic energy
M	Compressibility
ϵ	Dissipation rate
ω	Specific dissipation rate
ref	Reference variable
b	Buoyancy
eff	Effective variable
L	Corresponding to liquid fraction

Superscripts

$\overline{u}$	Average variable
$u^{'}$	fluctuating variable

Acronyms

CFD	Computational Fluid Dynamics
HVAC	Heating Ventilation & Air Conditioning
HTRC	Heat Transfer Coefficient

Contents

Contents

1 Introduction 1

2 Theory 2
2.1 Continuity and Momentum Equation . . . 2
2.2 Turbulence . . . 2
2.2.1 Reynolds Decomposition . . . 2
2.2.2 Boussinesq Hypothesis . . . 3
2.2.3 Realizable $k - \epsilon$ Model . . . 4
2.2.4 $k - \omega$ SST Model . . . 5
2.3 Heat Transfer . . . 6
2.3.1 Heat Transfer in Air Sub-domain . . . 6
2.3.2 Heat Transfer in Solid Region . . . 6
2.3.3 Heat Transfer in Ice Region . . . 7

3 Methodology 9
3.1 Computational Domain . . . 9
3.2 Meshing . . . 9
3.3 Mesh Independence Study . . . 11
3.4 Steady State Defroster Flow Simulation . . . 12
3.4.1 Define Material Properties . . . 12
3.4.2 Selection of Boundary conditions and Other Numerical Settings . . . 14
3.5 Transient Heat-up Defroster Simulation . . . 15
3.5.1 Boundary Conditions for Walls . . . 17
3.5.2 Thermal Properties of Air . . . 17
3.5.3 Convective Heat Transfer Coefficient . . . 17
3.5.4 Radiation effect due to High temperature walls . . . 17
3.5.5 Numerical Schemes . . . 18
3.5.6 Supply Heat Energy at the Heater . . . 18
3.6 Post-Processing . . . 18
3.7 Physical Test . . . 18

4 Results and Discussion 19
4.1 Defroster Flow Simulation Results . . . 19
4.2 Transient Heat-up Defroster Simulation Results . . . 23
4.2.1 Influence of boundary condition on the melting of ice . . . 23
4.2.2 Influence of thermal properties on the melting of ice . . . 26
4.2.3 Influence of convective heat transfer coefficient on the melting of ice . . . 28
4.2.4 Influence of radiation on melting of ice . . . 30
4.2.5 Influence of numerical schemes on the melting of ice . . . 32
4.2.6 Influence of heat energy supply on the melting of ice . . . 34

5 Physical Test Results 37
5.1 Correlation of Simulation Results to Physical Test Results . . . 37

6 Conclusion 39

7 Future Work 40

References 41

1 Introduction

Climate control plays a major role to enhance comfort and safety of the passengers in a car. Defroster system is one of the safety systems that falls under climate control system. The purpose of the defroster system is to melt the ice formed over the windscreen in a short duration of time. The defroster system is used to obtain the desired visibility on the windscreen for the driver before driving the vehicle. Air is inducted into plenum by a fan and passes through a HVAC unit. The HVAC unit consists of several components like evaporator and heaters which decreases absolute pressure of air while traverse across these components. The air also gains sufficient temperature across the heater with the help of a heating medium. The flow rate of the heated air is regulated using flaps in order to send the optimum air depending on the time required to defrost the ice over the windscreen and to comfort the passengers in the car. The air coming out from the HVAC unit enters in to defroster unit where the flow is split between the defroster outlet nozzles on the driver and passenger side in addition to side defrosters. Air coming out from these nozzles impinge on the windscreen and side windows and defrost ice in a short period of time.

Nowadays car manufacturers during the development stage analyse the performance of the defroster system using Computational Fluid Dynamics(CFD). With the use of CFD there is a considerable decrease in the development time. It is impossible to test all the defroster prototypes through physical tests as it demands enormous amount of time and cost in predicting the performance of the defroster prototypes. Therefore the car manufacturers utilize CFD in selection of efficient defroster model however its final performance is evaluated by conducting tests.

At Volvo Cars, CFD is used to develop and optimize various systems and attributes of the car. In the climate control system all the ducts are developed using CFD with regard of mass flow distribution and pressure drop. There has been great interest shown in correlation of defroster simulation results to the physical tests. There is a scope of improvement in predicting the performance of defroster through simulation methods. This master thesis is carried out to improve the accuracy of the current CFD method for windscreen deicing. Various modifications in terms of selection of boundary conditions, numerical schemes and turbulence models are made in order to predict the windscreen deicing accurately. Finally, defroster simulation results are correlated to the physical test results.

2 Theory

This chapter presents various transport equations used to solve fluid flow and heat transfer in the computational domain. The chapter begins with the description of the equations of motion of a continuum. Later the chapter extends with the illustration of Reynolds decomposition and Boussinesq hypothesis to compute average Reynolds stress. Moreover the transport equations of Realizable $k-\epsilon$ and $k-\omega$ SST turbulence model are described under turbulence section. Finally, energy equations used for solving thermal field in air, solid and ice sub domain are also explained.

2.1 Continuity and Momentum Equation

The first equation represents the continuity equation which is considered as law of conservation of mass.

$$\frac{\partial \rho}{\partial t} + \rho \frac{\partial u_i}{\partial x_i} = 0 \tag{2.1}$$

For incompressible flow (ρ = constant), the equation 2.1 can be written as

$$\frac{\partial u_i}{\partial x_i} = 0 \tag{2.2}$$

The momentum equation is used to solve three velocity components of the flow which is also referred to as law of conservation of momentum.

$$\frac{\partial u_i}{\partial t} + u_j \frac{\partial u_i}{\partial x_j} = -\frac{1}{\rho}\frac{\partial}{\partial x_i}p + \frac{\partial}{\partial x_j}\left(\nu \frac{\partial u_i}{\partial x_j}\right) + F_i \tag{2.3}$$

In the equation 2.3 the indices i,j = 1, 2, 3 and ρ refers to density and ν is the kinematic viscosity. F_i represents body force acting on the fluid. The equations 2.1 and 2.3 are commonly referred as Navier-Stokes equation. [1]

2.2 Turbulence

Most of the fluid flows that are seen in daily life are turbulent. For instance the flow around the vehicles and buildings are turbulent due to high Reynolds number [1]. It is practically impossible to resolve the flow with very high Reynolds number since it requires large computational resources. This is overcome by averaging the equations 2.1 and 2.3 using Reynolds averaging method. The average Reynolds stress is modelled using Boussinesq hypothesis in which turbulent variables are used for computing Reynolds stress. Furthermore turbulence model is required to compute turbulent variables like turbulent kinetic energy k, specific dissipation rate ω and dissipation rate ϵ, specific dissipation rate ω. These concepts used in modelling the turbulent flow are explained in this section.

2.2.1 Reynolds Decomposition

The instantaneous flow variables in the Navier-Stokes equation are decomposed into the mean and fluctuating variables (for example velocity components and pressure)[1]. As it requires larger computational resources and time to obtain instantaneous flow variables while solving the Navier-Stokes equations, it is better to decompose the flow variables into mean and fluctuating flow variables. Although it is possible to resolve all turbulent scales by solving the Navier-Stokes equations, it is not affordable in industrial flow computations.

$$u_i = \overline{u_i} + u^{'}_{\ i} \tag{2.4}$$

$$p = \overline{P} + p^{'} \tag{2.5}$$

In the equation 2.4, $\overline{u_i}$ represents the mean velocity and $u^{'}{}_i$ represents the fluctuating velocity which is similar for pressure mentioned in the equation 2.5. After averaging the continuity and momentum equations, the equations are written as

$$\frac{\partial \overline{u_i}}{\partial x_i} = 0 \tag{2.6}$$

$$\frac{\partial \overline{u_i}}{\partial t} + \overline{u_j}\frac{\partial \overline{u_i}}{\partial x_j} = -\frac{1}{\rho}\frac{\partial}{\partial x_i}\overline{P} + \frac{\partial}{\partial x_j}\Big(\nu\frac{\partial \overline{u_i}}{\partial x_j} - \overline{u_i^{'}u_j^{'}}\Big) + F_i \tag{2.7}$$

After time averaging, the equation 2.3 it is expressed as equation 2.7 which contains a new term $\frac{\partial}{\partial x_j}\big(\overline{u^{'}{}_i u^{'}{}_j}\big)$ known as the Reynolds stress tensor. It is to be noted that there are six Reynolds stresses which represent the correlation between the fluctuating velocities of the turbulent flow. The Reynolds stress which is a symmetric stress tensor has six unknown stress components. With the number of unknowns rising to ten, the number of equations are only four, thereby an assumption has to be made regarding the nature of the turbulent flow. This assumption is equivalent to determining six Reynolds stresses. [2]

2.2.2 Boussinesq Hypothesis

In the Boussinesq hypothesis, eddy viscosity is introduced to model the unknown Reynolds stresses. From this assumption it is possible to relate the Reynold stress to the mean velocity gradient.

$$\tau_{ij} = -\rho u_i^{'} u_j^{'} \tag{2.8}$$

$$\tau_{ij} = \mu_t\Big(\frac{\partial \overline{u_i}}{\partial x_j} + \frac{\partial \overline{u_j}}{\partial x_i}\Big) \tag{2.9}$$

where μ_t is the turbulent dynamic viscosity. It is to be noted that the equation 2.9 is not valid up on contraction and therefore the equation 2.9 can be written as

$$\overline{u_i^{'}u_j^{'}} = -\nu_t\Big(\frac{\partial \overline{u_i}}{\partial x_j} + \frac{\partial \overline{u_j}}{\partial x_i}\Big) + \frac{2}{3}\delta_{ij}k \tag{2.10}$$

where δ_{ij} is the kronecker's delta and k is the turbulent kinetic energy. The Boussinesq hypothesis, used in standard two equation turbulence models to compute turbulent viscosity μ_t, reduces the computational cost and time significantly. [3]

2.2.3 Realizable $k-\epsilon$ Model

The *Realizable* $k-\epsilon$ turbulence model [4] is similar to the standard $k-\epsilon$ model but this model has a new formulation for the turbulent viscosity. In addition to it, a transport equation for the dissipation rate, ϵ is derived from an exact equation for the transport of the mean-square vorticity fluctuation. The term *realizable* means that the model satisfies certain mathematical constraints on the Reynolds stresses [5].

An advantage of the *Realizable* $k-\epsilon$ model is that it accurately predicts the spreading rate of both planar and round jets. The performance of the model is better for flows having 3-d flow features like rotation, boundary layers under strong adverse pressure gradients, separation, and recirculation. One of the drawbacks in using the *Realizable* $k-\epsilon$ turbulence model is that it produces a non-physical turbulent viscosity in situations when the computational domain contains both rotating and stationary fluid zones. This is due to the consideration of mean rotation to compute turbulent viscosity. This additional rotation effect has been tested on a single reference frame systems and gave better performance than standard $k-\epsilon$ turbulence model [5]. The transport equation for k and ϵ are expressed in the equation 2.11 and 2.12

$$\frac{\partial}{\partial t}(\rho k)+\frac{\partial}{\partial x_j}(\rho k u_j)=\frac{\partial}{\partial x_j}\Big[\Big(\mu+\frac{\mu_t}{\sigma_k}\frac{\partial k}{\partial x_j}\Big)\Big]+G_k+G_b-\rho\epsilon-Y_M+S_k \tag{2.11}$$

$$\frac{\partial}{\partial t}(\rho \epsilon)+\frac{\partial}{\partial x_j}(\rho \epsilon u_j)=\frac{\partial}{\partial x_j}\Big[\Big(\mu+\frac{\mu_t}{\sigma_\epsilon}\frac{\partial \epsilon}{\partial x_j}\Big)\Big]+\rho C_1 S_\epsilon-\rho C_2\frac{\epsilon^2}{k+\sqrt{\mu\epsilon}}+C_{1\epsilon}\frac{\epsilon}{k}C_{3\epsilon}G_b+S_\epsilon \tag{2.12}$$

where

$$C_1=Max\Big[0.43,\frac{\eta}{\eta+5}\Big] \tag{2.13}$$

$$\eta=\frac{Sk}{\epsilon} \tag{2.14}$$

$$S=\sqrt{2S_{ij}S_{ij}} \tag{2.15}$$

The production of turbulent kinetic energy due to mean velocity gradients is given by

$$G_k=-\rho\overline{u'_i u'_j}\frac{\partial u_j}{\partial x_i} \tag{2.16}$$

The generation of turbulent kinetic energy due to buoyancy is calculated as

$$G_b=\beta g_i\frac{\mu_t}{Pr_t}\frac{\partial T}{\partial x_i} \tag{2.17}$$

In equation 2.17 Pr_t is the turbulent prandtl number for energy, g_i is the gravitational force vector in the direction i and β represents the coefficient of thermal expansion,

$$\beta=\frac{1}{\rho}(\frac{\partial\rho}{\partial T})_p \tag{2.18}$$

The constants used are:
$C_{1\epsilon}=1.44$; $C_2=1.9$; $\sigma_k=1.0$; $\sigma_\epsilon=1.2$; $\mathrm{Pr}_t=0.85$

It is to be noted that in the equation 2.11 and 2.12, S_k and S_ϵ represents user defined source terms. Y_M is the turbulence due to compressibility effects in the equation 2.11. One of the features of the production term present in the ϵ equation is that it does not involve the production of k thereby it represents the spectral energy transfer in a better way and moreover destruction term does not have any singularity. It is to be noted that *Realizable* $k-\epsilon$ model has been extensively tested for various types of flows including rotating homogeneous shear flows, free flows including jets and mixing layers, channel and boundary layer flows and separated flows [6].

2.2.4 $k-\omega$ SST Model

The shear stress transport(SST) $k-\omega$ model was developed by Menter [7]. This model effectively combines the robust and accurate formulation of the $k-\omega$ model in the near wall region with free-independence of the $k-\epsilon$ model in the far away from the wall [5]. This turbulence model is an eddy-viscosity model that limits the shear stress in the adverse pressure gradient regions which is over predicted by the $k-\epsilon$ turbulence model. Another drawback of the $k-\epsilon$ model is that it requires near-wall modifications. Whereas the limitation of the standard $k-\omega$ model is that the model is dependent on the free-stream value of ω [5]. These limitations are overcome by $k-\omega$ SST model. The $k-\omega$ SST turbulence model is similar to standard $k-\omega$ turbulence model but there are some changes in it. One of the change is that the blending function is multiplied with the standard $k-\omega$ and transformed $k-\epsilon$ turbulence model and added together. The blending function is designed to be one in the near wall region which enables the standard $k-\omega$ model and zero away from the surface, which enables the transformed $k-\epsilon$ turbulence model [5]. Moreover the $k-\omega$ SST turbulence model incorporates a damped cross diffusion derivative tem in ω equation and the definition of turbulent viscosity is modified to account for the transport of turbulent shear stress [5]. In addition to it, the modelling constants are different for both of the turbulence models.

These capabilities make the $k-\omega$ SST turbulence model more accurate and reliable for various types of flows (adverse pressure gradient flows, airfoils and transonic shock waves) than the standard $k-\omega$ model. Other changes include the addition of cross-diffusion term in the ω equation and the blending function to ensure that the model works well in the near-wall and far-field zones [5]. The transport equation for k and ω are specified as equations 2.19 and 2.20 respectively.

$$\frac{\partial}{\partial t}(\rho k)+\frac{\partial}{\partial x_i}(\rho k u_i)=\frac{\partial}{\partial x_j}\left[\left(\mu+\frac{\mu_t}{\sigma_k}\frac{\partial k}{\partial x_j}\right)\right]+G_k-\rho\beta^* k\omega+S_k \tag{2.19}$$

$$\frac{\partial}{\partial}(\rho\omega)+\frac{\partial}{\partial x_i}=\frac{\partial}{\partial x_j}\left[\left(\mu+\frac{\mu_t}{\sigma_k}\frac{\partial k}{\partial x_j}\right)\right]+G_\omega-Y_\omega+D_\omega+S_\omega \tag{2.20}$$

The production of turbulence kinetic energy is written as

$$G_k=min(G_k,10\rho\beta^* k\omega) \tag{2.21}$$

The term Y_k represents the dissipation of turbulent kinetic energy due to turbulence is computed as

$$Y_k=\rho\beta^* k\omega \tag{2.22}$$

The production of specific dissipation rate is given by

$$G_\omega=\alpha\frac{\omega}{k}G_k \tag{2.23}$$

The specific dissipation rate is calculated as

$$\omega=\frac{\epsilon}{\beta^* k} \tag{2.24}$$

It is to be noted that G_k is the production of turbulent kinetic energy, G_ω is the production due to specific dissipation rate, D_ω is the cross diffusion term and Y_ω represents the dissipation of ω due to turbulence. S_k and S_ω represents user defined source terms. The constant β^* in $k-\omega$ SST turbulence model corresponds to 1.

2.3 Heat Transfer

This section presents the energy equations used to compute the transient heat flow in various regions of the defroster domain. The section starts with the energy equation used in the domain occupied by air. The equation 2.25 computes the heat energy gained by the air across the heater is transferred to the windscreen when the flow coming out from the defroster outlet nozzle impinges on the windscreen. In addition to it, the equation 2.30 calculates the amount of heat energy gained by the windscreen from air and conducted across the windscreen which is then followed by convecting the heat towards the ice domain. The heat energy ejected out from the windscreen melts the modelled ice on the windscreen. Finally the equation 2.37 is used to evaluate the heat energy conducted through the ice region.

2.3.1 Heat Transfer in Air Sub-domain

The energy equation for the air is written as

$$\frac{\partial}{\partial t}(\rho E) + \nabla \cdot \Big(\vec{u}(\rho E + p)\Big) = \nabla \cdot \Big(k_{eff}\nabla T - \sum_j h_j \vec{J_j} + (\overline{\overline{\tau_{eff}}} \cdot \vec{u})\Big) + S_h \tag{2.25}$$

where k_{eff} represents the effective conductivity ($k_{eff} = k + k_t$, where k_t is the turbulent thermal conductivity, defined according to the turbulence model being used), $\vec{J_j}$ is the diffusion flux of species j. The three terms on the right hand side of the equation 2.25 represent the energy due to conductive heat transfer, species diffusion, and viscous dissipation, respectively [5]. S_h represents the heat source supplied at the heater.

$$E = h - \frac{p}{\rho} + \frac{u^2}{2} \tag{2.26}$$

where sensible enthalpy h is defined for ideal gases as,

$$h = \sum_j Y_j h_j \tag{2.27}$$

and for incompressible flows as

$$h = \sum_j Y_j h_j + \frac{p}{\rho} \tag{2.28}$$

In equations 2.27 and 2.28, Y_j is the mass fraction of species j and

$$h_j = \int_{T_{ref}}^{T} c_{pj}\, dT \tag{2.29}$$

where T_{ref} is 298.15 K.

2.3.2 Heat Transfer in Solid Region

The following energy transport equation is used for computing the heat transferred by the windscreen from the region occupied by air to ice.

$$\frac{\partial}{\partial t}(\rho h) = \frac{\partial}{\partial x_i}\Big(k\frac{\partial T}{\partial x_i}\Big) \tag{2.30}$$

In the equation 2.30 the left side term represents the heat convected to or from the windscreen and the right side term represents the heat conducted across the windscreen.

2.3.3 Heat Transfer in Ice Region

The Enthalpy-porosity methodology [8] is used to model the melting of ice on the windscreen. This approach uses the enthalpy formulation in which case no explicit conditions on the heat flow at the solid-liquid interface need to be accounted for and therefore the potential arises for a solution to model the melting process [9].

The computational cells in which a phase change is occurring are modelled as pseudo porous media with the porosity, λ, increasing from 0 to 1 when the mean latent heat $\triangle H$ increases from 0 (cell all solid) to L (cell all liquid) [10]. Furthermore, the approach considers that the ice melts over a temperature range $\epsilon \leq T \leq -\epsilon$ where ϵ and $-\epsilon$ refers to liquidus and solidus temperature respectively. The solidus temperature refers to the temperature at which the ice begins to melt and the liquidus temperature means that at this temperature the ice is completely melted into water. This approach considers that the evolution of latent heat as a functional relationship with the temperature $\triangle H = f(T)$ as opposed to step change associated with an isothermal phase change [9]. Problems of this type are referred to as mushy region problems to indicate the solid plus liquid state of the material in the phase-change range.

The mushy region is also considered as a region in which the liquid fraction varies from 0 to 1. It is to be taken into account that the melt interface is not tracked explicitly in this technique. The enthalpy porosity approach exists as Solidification and Melting model in *Ansys Fluent* [5]. The enthalpy of the material is computed as the sum of the sensible enthalpy, h, and the latent heat, $\triangle H$

$$H = h + \triangle H \tag{2.31}$$

$$h = h_{ref} + \int_{T_{ref}}^{T} c_p dT \tag{2.32}$$

where
h_{ref} = reference enthalpy
T_{ref} = reference temperature
c_p = specific heat at constant pressure

The liquid fraction, β_L, can be defined as

$$\beta_L = 0 \tag{2.33}$$

If $T < T_{solidus}$

$$\beta_L = 1 \tag{2.34}$$

If $T > T_{liquidus}$

$$\beta = \frac{T - T_{solidus}}{T_{liquidus} - T_{solidus}} \tag{2.35}$$

If $T_{solidus} < T < T_{liquidus}$

The equation 2.35 is referred to as the lever rule. The latent heat content is computed using liquid fraction and mean latent heat as

$$\triangle H = \beta_L L \tag{2.36}$$

For solidification and melting problems, the energy equation is written as

$$\frac{\partial(\rho H)}{\partial t} + \nabla \cdot (\rho \vec{u} H) = \nabla \cdot (k \nabla T) + S_L \tag{2.37}$$

where
H = enthalpy

ρ = density
$\vec{u}$ = fluid velocity
S_L = source term

The momentum sink due to reduced porosity in the partially melted ice region takes the following form [5]

$$S_L = \frac{(1-\beta_L)^2}{({\beta_L}^3 + \epsilon_L} A_{mush}(\vec{v} - \vec{v_p}) \tag{2.38}$$

In the equation 2.38, ϵ_L is a small number (0.001) to prevent division by zero, A_{mush} is the mushy zone constant and $\vec{v_p}$ is the pull velocity (which is set as zero). Moreover the mushy zone constant measures the amplitude of damping [5]. A_{mush} values range between 10^4 and 10^7.

It is to be noted that the solution for temperature is essentially an iteration between the energy equation 2.37 and the liquid fraction equation. Using 2.35 to update the liquid fraction results in poor convergence of the energy equation. In $ANSYS\ fluent$ the following liquid fraction correction equation is used to update the liquid fraction.

$$[\beta_L]^{k+1} = [\beta_L]^k + \lambda[\triangle\beta_L] \tag{2.39}$$

where
$[\beta_L]^{k+1}$ = computed liquid fraction for k+1 iteration
$[\beta_L]^k$ = computed liquid fraction for k iteration
λ = under relaxation factor
$[\triangle\beta_L]$ = liquid fraction correction for k+1 iteration

3 Methodology

This chapter presents the methodology adopted to perform CFD simulations so that the melting pattern of ice obtained from the simulation can be compared with the physical test results. The chapter begins with a description of the computational domain and then the generation of surface and volume mesh for the defroster domain. The mesh independence study section delivers the information on how the influence of mesh on the simulation results is eliminated. Moreover, steady state defroster flow simulation section presents the information required to execute various pre-processing steps thereby the defroster flow impinging on the windscreen can be analysed before performing transient thermal analysis. Furthermore, transient heat-up simulation section provides necessary information to perform transient thermal analysis. The post-processing section specifies the softwares used to analyse the simulation results. Finally, the chapter ends with the the description of the physical test executed at Volvo Cars.

3.1 Computational Domain

Volvo V40 cabin model is used to generate the computational domain. The inlet of the computational domain is the inlet of HVAC unit which includes porous components such as evaporator, heater and PTC (additional heater used only in Cars sold in cold countries). The temperature doors in the HVAC unit are positioned in such a way that the air flowing through the HVAC unit passes only through heater and PTC. The floor doors in the HVAC unit blocks air so that the flow occurs only through defroster duct. The defroster unit connected to downstream of the HVAC unit splits the incoming flow to driver and passenger defroster ducts. Later the flow discharging from the defroster nozzles enters into cabin and finally discharges at the outlet present at the rear end of the car.

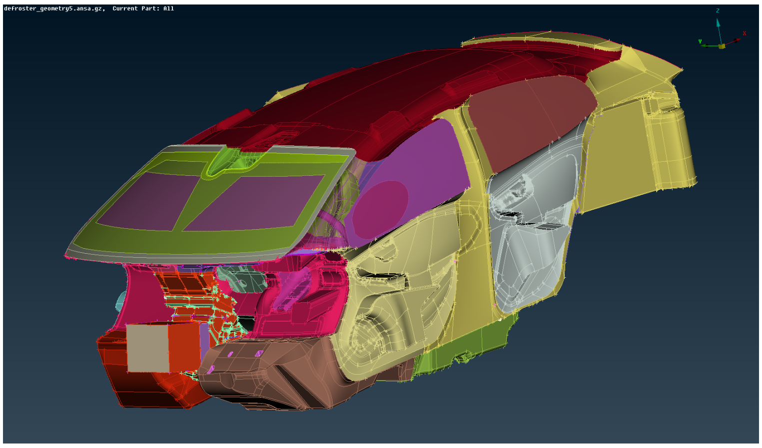

Figure 3.1: *3-D View of Volvo V40 cabin model*

3.2 Meshing

Meshing is accomplished to discretize the computational domain into n number of cells over which partial differential flow equations are approximated. In this thesis, the domain is initially surface meshed in $ANSA$ and then volume mesh is generated using $HARPOON$ meshing software. Finally windscreen and ice are generated as prism layers over the cabin surface interface with the windscreen using $fluentmesh$. The strategy used to generate surface and volume mesh are discussed in detail in the next section.

The Volvo V40 CAD model is examined initially to ensure that all the faces are connected to their neighbour faces. The CAD clean-up is performed to generate a well defined surface mesh. The purpose of the surface mesh is to preserve geometric features before generating the volume mesh. The CAD model is a 3-d complex geometry which lead to the selection of triangular mesh elements. The element size is varied from 0.5 *mm* to 16 *mm* over the shells of all components in the domain to generate unstructured surface mesh. Several surface mesh models with different cell sizes are created to conduct mesh independence test. The meshing tool *ANSA* is used to generate the surface mesh.

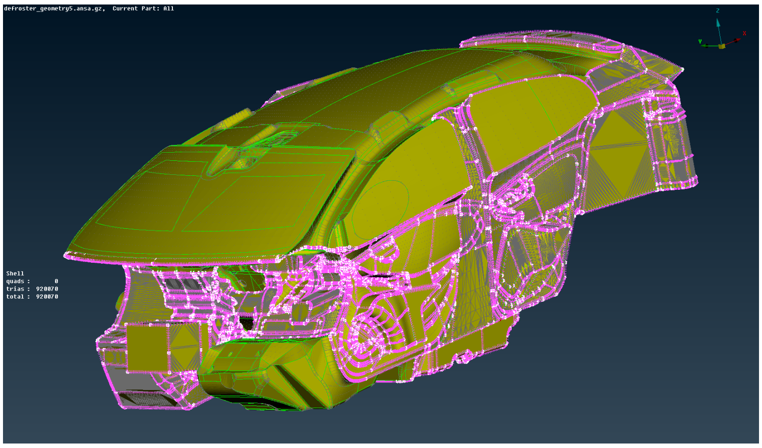

Figure 3.2: *Surface mesh generated over the computational domain*

The surface mesh generated using *ANSA* acts as a representation of geometry when the output file is imported in to *Harpoon*. The volume mesh generated using *Harpoon* meshing tool starts to generate mesh from the centre of the domain and grows in the outward direction. The mesh growth is inhibited by the surface mesh and *Harpoon* generates a surface mesh at the intersection between the volume mesh and surface mesh using *ANSA*. Since the accuracy of the simulation results are of high importance, it is necessary to have either a hexahedral or polyhedral mesh which offers high density and captures all the flow features in the domain. Therefore hexahedral mesh is used to generate volume mesh. The density of the mesh is also controlled using "plevel" and "pexp" features in *Harpoon* which assists to specify surface cell length and cell growth in the domain. The interface surfaces between the components in the entire domain are set as *radiator* which refers to interface, assists to extract defroster flow and thermal field data while analysing the simulation results. Boundary layers are considered on the windscreen and side windows since the flow coming out from the defroster nozzle attaches to the windscreen. It is to be noted that the windscreen and ice layer over the cabin surface interfaced with windscreen is also a part of the computational domain which doesn't exist in the CAD model. The modelling of these sub domains is accomplished using *Fluentmesh* by generating prism layers. With the help of prism layers, these regions have a uniform cell size throughout the respective sub-domains. This is essential in order to accurately predict the melting pattern of ice on the windscreen. Figure 3.3 shows the volume mesh generated for the defroster computational domain which also includes the modelled windscreen and ice.

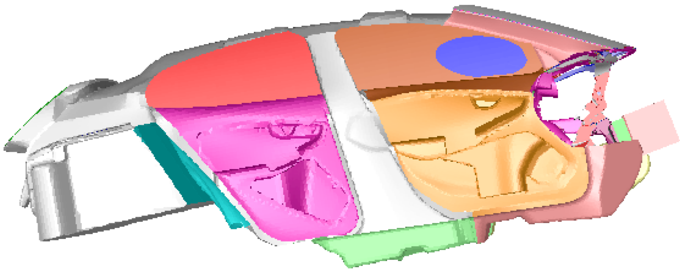

Figure 3.3: *Volume mesh for the defroster domain*

3.3 Mesh Independence Study

The mesh independence study is performed so that the simulation results does not have the influence of mesh quality. In this study, several meshes with various element size are analysed to identify the coarsest mesh which does not influence the simulation results to a considerable extent. Furthermore, total pressure at one of the defroster outlet nozzles was considered for analysing the simulation results. In addition to total pressure, y^+ at windscreen and side windows is also taken into account during the slection of mesh. The relative pressure is calculated by comparing the total pressure obtained for a specific mesh to the total pressure obtained for a mesh having 169 million cells. It was found that, when the total number of cells were around 50 million cells, the influence of mesh quality on the simulation results reduced drastically which is shown in fig 3.1. However, the mesh having 110 million cells was chosen to carry out the simulations as there was a minor improvement in y^+ when compared to a mesh with 50 million cells. Moreover, the $k - \omega$ *SST* turbulence model used for solving the defroster flow field is very sensitive to y^+ and it is recommended to have y^+ less than 5 at the regions having large gradients. Once this study is accomplished, steady state defroster flow simulations can be carried out.

Table 3.1: Mesh Independence Study Results

Total number of cells (in millions)	Percentage change in total pressure	Y^+ at windscreen and side windows
5	80.8	21.39
6	67.3	8.36
50	5.08	5.49
110	1	5.14
136	6.63	5.01
169	–	4.97

3.4 Steady State Defroster Flow Simulation

The steady state defroster flow simulation is performed to analyse the air flow distribution over the windscreen. Having a uniform flow field contributes to better heat transfer across the windscreen and eventually leads to quicker melting of ice. It is recommended to have the velocity around 2.5 m/s for the flow which is attached to the windscreen. This is achieved by initially assigning the thermal properties for solid and fluid materials applicable to the respective sub-domains.

3.4.1 Define Material Properties

The materials considered before performing steady state defroster flow simulations are shown in the table 3.2,3.3,3.4 and 3.5

Table 3.2: Thermal Properties of Glass

Property	Value
Density (kg/m^3)	2500
Specific heat capacity (J/kgK)	750
Thermal Conductivity (W/mK)	0.8

Table 3.3: Thermal Properties of Plastic

Property	Value
Density (kg/m^3)	1000
Specific heat capacity (J/kgK)	1980
Thermal Conductivity (W/mK)	0.2

It is to be noted that the windscreen is made by sandwich plastic material whose thickness is 0.76 mm between the glass of thickness 2.1 mm and 2.6 mm respectively. The thermal properties of glass and plastic are listed in the table 3.2 and 3.3 respectively.

Table 3.4: Thermal Properties of Air

Property	Value
Density (kg/m^3)	1.225
Specific heat capacity (J/kgK)	1006
Thermal Conductivity (W/mK)	0.0242
Dynamic Viscosity (Ns/m^2)	1.7894e-05

Table 3.5: Thermal Properties of Ice

Property	Value
Density (kg/m^3)	920
Specific heat capacity (J/kgK)	2040
Thermal Conductivity (W/mK)	1.88
Dynamic Viscosity (Ns/m^2)	0.00533
Latent heat of fusion (J/kg)	333.55
Solidus Temperature (K)	271
Liquidus Temperature (K)	273
Latent heat of melting (J/kg)	334960

Table 3.4 represents the thermal properties of air that are used for the steady state flow and transient thermal defroster simulations. In addition, Table 3.5 shows various thermal and two-phase properties of ice that are considered while performing steady state flow and transient heat-up simulation. It is to be noted that ice domain is considered to have a thickness of 0.46 mm. Furthermore, the components namely the evaporator, heater and PTC are regarded as porous media and properties like viscous resistance and

inertial resistance are specified based on the available data.

3.4.2 Selection of Boundary conditions and Other Numerical Settings

The next step in pre-processing of steady state defroster flow simulation is to specify boundary conditions. A constant mass flow rate corresponding to 100 l/s is specified initially at the inlet of the HVAC unit and pressure outlet with a zero gauge pressure (bar) is specified at the outlet of the computational domain. The other boundaries of the domain are set as walls by default. Once the boundary conditions are specified, a turbulence model is chosen to model turbulence in the defroster flow field. In this project, the turbulent flow is modelled using the *Realizable* $k-\epsilon$ and $k-\omega$ SST turbulence models. In addition, the flow field near the walls is solved accurately by generating the boundary layers on the HVAC and defroster duct walls, and this is also achieved by enabling the *enhance wall treatment model* along with a turbulence model. Later, the second order upwind scheme is selected to discretize flow and turbulent transport equations. Depending on the turbulence model, the flow variables (pressure, velocity) and turbulent flow variables like turbulent kinetic energy, specific dissipation and dissipation are initialized to zero. Furthermore, the flow variables are monitored at all the interfaces in HVAC and defroster units. This assists to verify that the flow is conserved in all the sections of the domain. Finally, the continuity and momentum equations are solved for the defroster flow field. Once the steady state solution is converged, the simulation results are post-processed using $EnSight$. The parameters such as the velocity and the heat transfer coefficient are approximated based on shear stress and turbulent kinetic energy are analysed on the windscreen.

It is to be noted that the apparatus used to monitor the flow rate of the heating medium during the physical test was found to have an issue which hindered air mass flow rate and heat energy calculation across the heater. It was later provided by the testing team from a new test performed using Volvo V40. Due to this delay in obtaining heating medium flowrate data, it was necessary to simulate the defroster flow simulation with a mass flow rate corresponding to 70, 80, 90, 100 and 112 l/s in order to predict the actual mass flow rate of air existed during the tests. Having simulated the defroster flow using various mass flow rate, the selection of appropriate mass flow rate is selected which will be discussed in the section 4.1.

3.5 Transient Heat-up Defroster Simulation

Transient heat-up simulation is performed to determine the amount of time required to melt ice completely on the windscreen and to visualize the melting pattern of ice at various intervals of time. The internal windscreen temperatures obtained form the simulation would be useful to validate the physical test results. The transient heat-up simulation can be performed by enabling the $solidification\ and\ melting$ model which solves the energy equation in the domain [5].. It is to be noted that the equations corresponding to flow and turbulent variables are not solved during the transient heat-up simulation. In addition, a convective boundary condition is applied at the external boundary of ice which is in contact with the surroundings. The convective heat transfer coefficient value used in the simulation was determined from previous tests. The temperature profile obtained at the outlet of HVAC unit during physical test was applied at the inlet of the HVAC unit while executing the transient heat-up simulation. The other boundaries of the domain are set with an adiabatic thermal boundary condition. Before solving the energy equation, temperature of $255.15K$ was initialized throughout the domain which was also the temperature of the climatic cold chamber. An implicit time stepping method with multiple time steps was chosen for all the transient heat-up CFD models. Various CFD models shown in table 3.6 were analysed and compared with the physical test results. The following transient heat-up defroster models are described in the following sections.

Table 3.6: Various Transient Thermal CFD models

Model	A-pillar, IP, Front doors	Air Properties	Convective HTRC (w/m^2K)	Radiation effect	Numerical Scheme	Heat Source
A	adiabatic	constant	8.6	no	unsteady first order	transient temperature
B	$255.15K$	constant	8.6	no	unsteady first order	transient temperature
C	transient temperature	constant	8.6	no	unsteady first order	transient temperature
D	transient temperature	$f(T)$	8.6	no	unsteady first order	transient temperature
E	transient temperature	$f(T)$	0	no	unsteady first order	transient temperature
F	transient temperature	$f(T)$	4.3	no	unsteady first order	transient temperature
G	transient temperature	$f(T)$	17.2	no	unsteady first order	transient temperature
H	transient temperature	$f(T)$	8.6	yes	unsteady first order	transient temperature
I	transient temperature	$f(T)$	8.6	no	unsteady second order	transient temperature
J	transient temperature	$f(T)$	8.6	no	unsteady second order bounded	transient temperature
K	transient temperature	$f(T)$	8.6	no	unsteady first order	Heat energy

3.5.1 Boundary Conditions for Walls

It is interesting to know the influence of change in boundary conditions on the transient simulation results. Therefore thermal boundary conditions on certain walls like A-pillar, Instrument panel (IP) and front doors are modified from adiabatic ($model\ A$) to having constant temperature of $-18°C$ ($model\ B$) and later providing transient temperature profile ($model\ C$) obtained from the physical test.

3.5.2 Thermal Properties of Air

The impact of temperature on the transient simulation results is analysed by comparing a CFD model ($model\ C$) with constant thermal properties of air to a model where the thermal properties of air are set as a function of the temperature ($model\ D$). It is to be noted that the rest of the pre-processing set up for both the models are same as mentioned in 3.5 except that the transient temperature profiles are specified for the walls like A-pillar, IP and front doors. The following properties are considered to be temperature dependent for the latter model in which T represents the temperature of the air and T_{Ref} represents the reference temperature of 273 K.

Table 3.7: Thermal air properties as a function of temperature

Property	Function
Density (kg/m^3)	$1.2895 - 0.0044 \times (T - T_{Ref}) + 1e - 05 \times (T - T_{Ref})^2$
Specific heat capacity (J/kgK)	$1.005 + 4e - 19 \times (T - T_{Ref})$
Thermal Conductivity (W/mK)	$0.0242 + 7e - 05 \times (T - T_{Ref})$
Dynamic Viscosity (Ns/m^2)	$17.169 + 0.05 \times (T - T_{Ref})$

3.5.3 Convective Heat Transfer Coefficient

Since the accuracy of the transient models can be measured on how well the melting pattern of ice matches with the physical test results, it becomes essential to analyse the significance of selection of the convective heat transfer coefficient over the outer boundary of ice. Transient models with different convective heat transfer coefficients (0, 4.3, 8.6, 17.2 w/m^2k) are considered and the remaining pre-processing set-up of transient CFD simulations are same as model D. The transient CFD models with convective heat transfer coefficient of 0, 4.3, 8.6 and 17.2 W/m^2k corresponds to $model\ E$, F, D, G respectively.

3.5.4 Radiation effect due to High temperature walls

The effect of radiation on the transient simulation results are analysed since the temperature of the A-pillar, IP and front door walls vary from $-17\ °C$ to $20\ °C$ with respect to time. This is carried out by selection of radiation model $surface - to - surface$ which is referred as ($model\ H$) and other pre-processing set up for the transient CFD models are similar to $model\ D$. These two transient models are analysed in order to realize the significance of radiation phenomenon in the defroster domain.

3.5.5 Numerical Schemes

In order to further improve the accuracy of a CFD model, it is important to analyse the influence of discretization schemes used for the advection and conduction heat transfer terms, while solving the energy equation. An improper choice of numerical scheme leads to the loss of information due to numerical diffusion and other numerical errors. Therefore, transient heat-up CFD models with different numerical schemes, namely unsteady first order (*model D*), unsteady second order (*model I*) and unsteady second order with bounded schemes (*model J*) are selected to discretize the energy equation.

3.5.6 Supply Heat Energy at the Heater

With the mass flow rate of heating medium known, it is possible to calculate the amount of heat supplied by the heating medium to air when it flows across the heater. As the heat is gained gradually by the heating medium from the engine, it is appropriate to provide a transient heat energy at the heater. The heat energy supplied as heat energy per unit volume (*model K*) by changing the thermal boundary condition for the heater. It is to be noted that the temperature of air at the inlet of the HVAC unit was modified and provided a constant temperature of 255.15 K. This transient model is set-up to view the difference in the simulation results from the model D where temperature profile is provided at the inlet of the HVAC unit.

3.6 Post-Processing

The post-processing of the steady state defroster flow simulations and transient heat-up simulations are carried out by using *Ensight* post-processing software and by creating monitors in *ANSYS Fluent*. The in-house python script was available to post-process the simulation results using *Ensight*. The velocity iso-surfaces and heat transfer coefficient contours on the windscreen were used to analyse the steady state defroster flow simulation results. In addition, monitors were set to record the average liquid fraction, average ice temperature, windscreen temperature on driver and passenger side.

3.7 Physical Test

This section presents the information to perform defroster test according to *SAE J902A* [11]. There are several test equipments used for conducting the test and some of the important equipments are stopwatch, thermocouples, spray gun to spray the water on the windscreen, burette to measure the quantity of water and an orifice meter to measure the flow rate of heating medium passing across the heater. It is to be noted that the test chamber temperature is maintained around $-18°C$ and air velocity of 1 mph is directed at the windscreen. The engine speed is maintained at 1500 rpm throughout the test. Volvo V40 used to perform the defroster test is soaked for at least 10 hours in the chamber with a temperature of $-18°C$. Before starting the test, the ice is coated over the windscreen with the help of a spray gun. The water is sprayed that the 0.046 $ml(of\ water)/cm^2$ is applied over the glass area with a pressure of 45 to 55 psi. After the ice is sprayed over the windscreen, the test is started within 30 minutes. The temperature of the air is measured at various locations in the HVAC unit, defroster unit, cabin and on windscreen. It is essential to monitor the temperature of the air across the heater and heating medium flow rate so that the heat gained by air can be calculated and this data can be fed as a heat energy source while simulations are carried out. In addition to it, the temperature monitored at defroster outlet nozzles assists at later stage to know the variation in temperature of air as it passes from heater outlet till it reaches defroster outlet. Moreover,the windscreen temperature monitored during the test assists in validating the simulation results. During the test, melting pattern of ice is monitored and recorded after every 5 minutes. The total duration of the test is carried out for 30 minutes. [11]

4 Results and Discussion

This section presents the results of steady state defroster flow and transient heat-up simulation. The steady state simulation is executed to ensure that the defroster flow impinging on the windscreen is uniformly distributed around the windscreen. Later the transient simulation results gives information about the performance of various models and their correlation to the physical test results.

4.1 Defroster Flow Simulation Results

After post-processing the steady state defroster flow solution, it is essential to predict the mass flow rate of air to ensure that the simulated flow corresponds to the actual flow inducted into HVAC and defroster units during the test. This is achieved by extracting the defroster outlet temperature data from the simulation results. Figure 4.1 shows the defroster outlet temperature profile for various mass flow rates specified at the inlet of the HVAC unit. It is concluded that the temperature profile obtained from the physical test correlated well with the profile having mass flow rate corresponding to 100 l/s however there is a constant offset between the profiles. Later with the heating medium flow rate data provided by the testing team, it was possible to calculate the average volume flow rate of air which was approximately 100 l/s. It is to be noted that the defroster outlet temperature obtained from the simulation results did not exactly match with the test results since the heat consumed to raise the temperature of the components in HVAC and defroster units was not considered. This flow rate data was also later utilized to perform transient heat-up simulations.

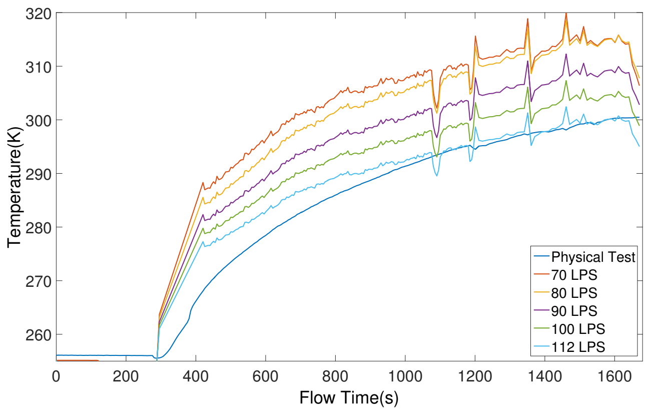

Figure 4.1: *Defroster outlet temperature profile for various mass flow rate of air*

It is also found that the flow coming out from the defroster nozzle impinges on the windscreen and attaches till the flow travels over the top of the windscreen. It is seen from Figure 4.2 that the defroster flow with a velocity of 2 m/s is distributed almost completely over the windscreen whereas the flow with a velocity 3 m/s prevails only in the region close to the flow impingement points.

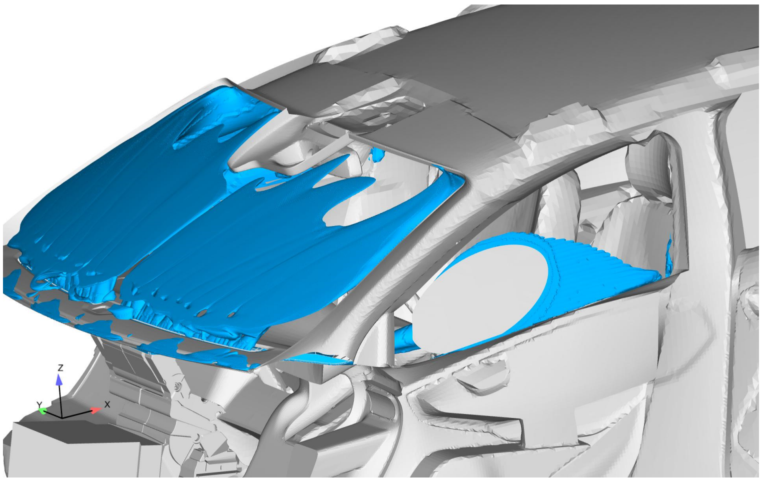

Figure 4.2: *Isometric view of flow with a velocity magnitude* 2 m/s *impinging windscreen and side windows*

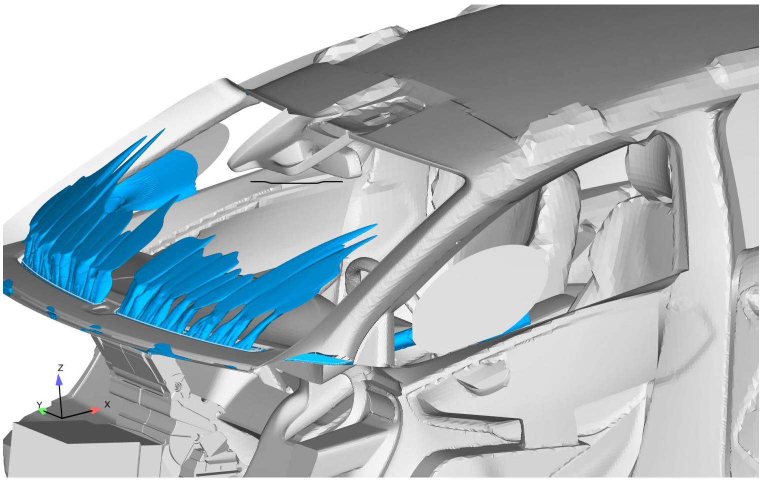

Figure 4.3: *Isometric view of flow with a velocity magnitude* 3 m/s *impinging windscreen and side windows*

There is a large rise in temperature in defroster flow impingement regions when compared to other regions in the windscreen. This can be related to heat transfer coefficient ($HTRC$) contour where HTRC is very high (around 50 w/m^2k) at these regions and decreases gradually as the flow passes to the top of the windscreen which is displayed in the figure 4.4. The heat transfer coefficient contour (Figure 4.4) as obtained based on the parameters like the turbulent kinetic energy, shear stress and skin friction coefficient provides a preliminary information about the heat transfer across the windscreen. From Figure 4.4 it is believed that there will be high transfer of heat at the locations close to the defroster flow impingement region as there is a higher heat transfer coefficient and vice versa at the locations far away from the defroster flow impingement region.

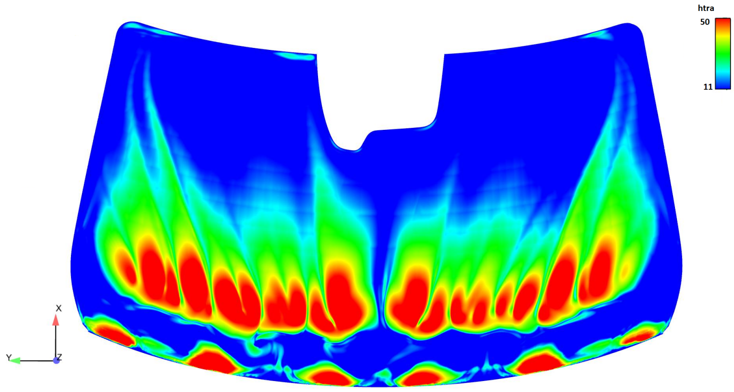

Figure 4.4: *Heat transfer coefficient contour on windscreen*

One interesting thing is that by creating the vertical planes across different sections of the defroster nozzle, it is found that there is a small recirculation region at the lower flow impingement region which can be observed in Figure 4.5. Due to the presence of a recirculation region the defroster outlet flow does not hit the windscreen at this small region. Instead, the flow glides past the recirculation region and attaches to the windscreen. In addition, there are four defroster outlet leak nozzles present at the driver and passenger sideS which allows for the flow to hit at the bottom of the windscreen. Due to the defroster leak flow there are eight circular sections of higher heat transfer coefficient at the bottom of the windscreen, as shown in figure 4.4. The higher heat transfer coefficient at eight circular regions leads to the quicker melting of ice on the windscreen and this would eventually assist the visibility of the driver. The leak nozzles are intended only to melt the ice at the bottom of the windscreen. It is to be noted that the discussions related to the steady state defroster flow simulation results are done when *Realizable* $k-\epsilon$ turbulence model is used to simulate the flow.

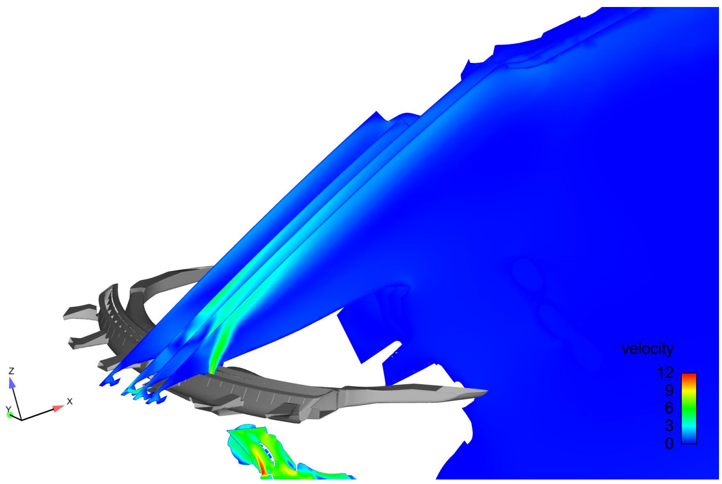

Figure 4.5: *Velocity contour on vertical plane using Realizable* $k-\epsilon$ *model*

Figure 4.6 shows the vertical plane cut across the defroster outlet nozzle for the steady state defroster flow simulation using the $k-\omega$ SST turbulence model. From Figure 4.6 it is concluded that the recirculation region at the impingement point is reduced to a great extent when compared to the one found in Figure 4.5. Furthermore, the flow at certain regions in the passenger and driver defroster ducts reach to a velocity magnitude of 12 m/s and shows that there is no uniform flow field whereas there is no such large gradients in the flow observed for *Realizable* $k-\epsilon$ turbulence model results. As the flow glides past the windscreen, a small lump of flow with a velocity of magnitude of 3 to 4 m/s is found at the downstream of the attached flow which is a non-physical result. This non-physical flow behaviour is because that the continuity equation has not converged sufficiently. By comparing the simulation results obtained for these turbulence models, it is concluded that the Realizable $k-\epsilon$ model suits well for carrying out the steady state defroster flow simulations.

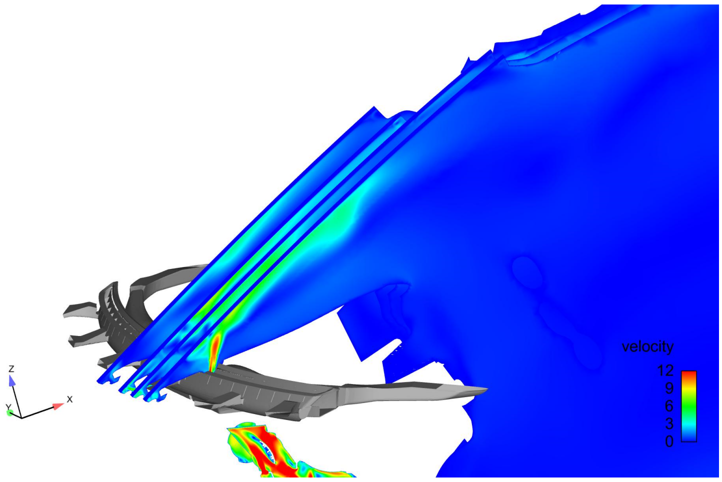

Figure 4.6: *Velocity contour on vertical plane using* $k-\omega$ *SST model*

4.2 Transient Heat-up Defroster Simulation Results

This section presents the influence of change in boundary conditions and other numerical settings on various transient heat-up defroster simulation results. The parameters like the average ice temperature, average liquid fraction (β) and windscreen temperature are monitored to assess the performance of transient CFD models. Finally, the transient CFD simulation results are correlated to the physical test results.

4.2.1 Influence of boundary condition on the melting of ice

This section presents the information about the transient simulation results when the boundary conditions are modified for certain walls like A-pillar, IP and front doors. The performance of the transient models is discussed after the description of the nature of average temperature and liquid fraction profiles at the external boundary of ice. From Figure 4.7, it can be seen that the temperature at the outer boundary of ice remains at 255.15K for nearly 360 seconds. The absence of rise in temperature until 360 seconds can be attributed to the amount of time consumed for the air to gain heat at the heater and later to undergo a conductive heat transfer across the windscreen. The transient temperature provided at the inlet of the HVAC unit has begun to increase after 300 seconds, which eventually takes additional 60 seconds for the rise in temperature at the ice boundary. From Figure 4.7 it can be seen that, after 360 seconds, there is a gradual rise in temperature over the external ice boundary until the temperature reaches around 282 K. This observation confirms that the melting occurs in the domain within this corresponding interval of time.

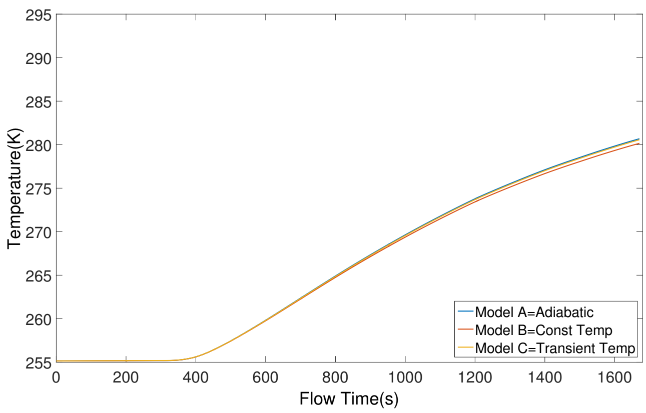

Figure 4.7: *Average temperature at the external boundary of ice*

The rise in temperature at the boundary of ice has a direct influence on the melting of ice and this can be noticed in Figure 4.8. This is done by monitoring the average liquid fraction over the ice boundary. The β begins to rise when flow time is approximately 840 seconds, which is due to consumption of time to gain heat for the air at the heater, conduct heat across the windscreen and to rise temperature from 255 to 273 K in the ice sub domain. Once β reaches 1, it is ensured that the ice is completely melted over the windscreen and therefore β curve flattens out.

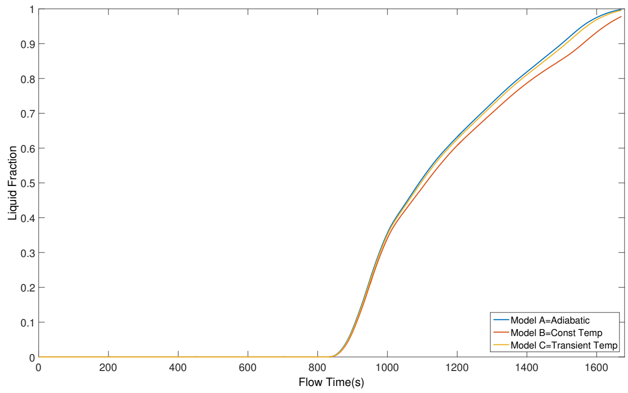

Figure 4.8: *Average liquid fraction, β_L at the external boundary of ice*

It is found from Figures 4.7 and 4.8 that there is a minor influence on the average temperature and liquid fraction at the outer boundary of ice when the boundary conditions are varied from adiabatic (model A) to constant temperature of $-18°C$ (model B)and then to a transient temperature profile (model C). Furthermore, it can be seen that there is no significant impact on the average temperature and liquid fraction when the thermal boundary condition is modified from adiabatic to transient temperature profile at the mentioned walls. Furthermore it is clearly visible that the model B average temperature and liquid fraction profiles slightly deviate from the other models. This can be discarded since the walls are specified with a constant temperature of $-18°C$, which cannot be considered as an appropriate boundary condition. These observations are also found by monitoring the liquid fraction and total temperature contours at various intervals of time. Figure 4.9 also shows that the melting has started to occur only at the region around the flow impingement points and that there is no major difference in the melting pattern of ice between the models.

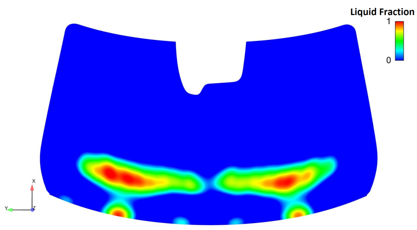

(a)

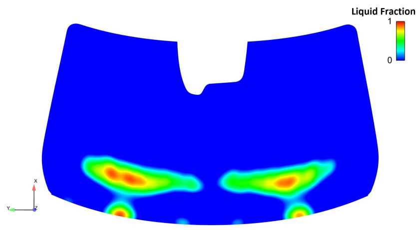

(b)

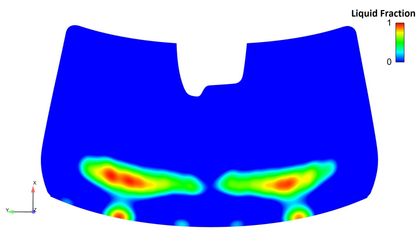

(c)

Figure 4.9: *Liquid fraction β_L contour for Models with adiabatic (a), constant temperature $255K$ (b) and transient temperature (c) boundary condition at the end of 900 seconds*

In order to measure the accuracy of the transient CFD models with respect to defroster test, the windscreen temperatures are monitored at the locations close (Location A shown in the figure 4.10) and far away (Location B shown in the figure 4.10) from the flow impingement region. The ratio of the difference in the internal windscreen temperature between any transient CFD model and model A to the difference in temperature between the defroster test & model A is used to calculate the accuracy of the transient defroster CFD models. When the difference in temperature between a transient model and model A is divided by the difference in temperature between model A and physical test and this resultant is multiplied over 100 provides how accurate the transient CFD models when compared to model A. The calculated accuracy value can also be used to measure the performance of the models relative to test. It was found that the model B accuracy is approximately 15 % and model C accuracy by around 7% at the location close to the defroster flow impingement points. In the same time, the accuracy of the model B and C are nearly 52% and 18 % respectively (with respect to model A) at the location far away from the flow impingement points. Although the accuracy of the model B is greater than the model C, it was concluded that the model C will be used to further improve accuracy of the CFD model since the temperature of the walls used in the model C represents the temperature of the respective walls from the physical test.

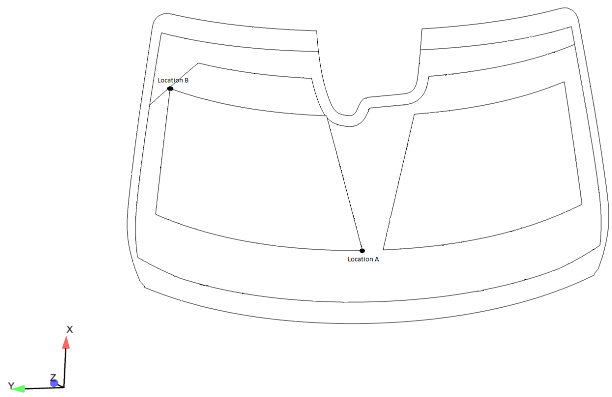

Figure 4.10: *Locations on the windscreen used to monitor temperature*

4.2.2 Influence of thermal properties on the melting of ice

The influence of thermal properties of air on the simulation results are discussed in this section. The nature of temperature profile for both the transient models (shown in the figure 4.11) is similar. However, there is a small offset in the profile between the two models and the average temperature rise for model D is higher than model C due to the consideration of properties as a polynomial function of the temperature. It is to be noted that the average temperature and liquid fraction profiles are similar to the profile shown in the section 4.2.1.

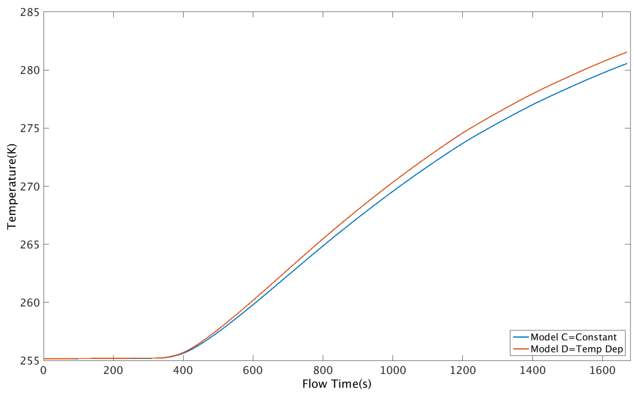

Figure 4.11: *Average temperature at the external boundary of ice*

The reason for the rise in temperature at the boundary of ice with respect to melting of ice is the same as described in the section 4.2.1. From Figure 4.12 it can be observed that the ice melts quicker for the model D than model C until β reaches 0.7.

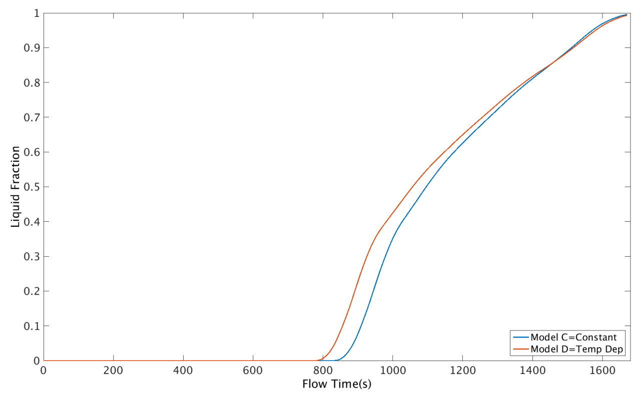

Figure 4.12: *Average liquid fraction, β_L at the external boundary of ice*

From Figure 4.13 it can be interpreted that the phase change is completely manifested over the defroster flow impingement regions for model D whereas in model C the melting of ice has started to initiate at the flow impingement regions. Moreover, by observing the liquid fraction contours at various intervals of time it was found that that the melting of ice begins at the regions where the defroster flow is impinged on the windscreen and later the melting occurs around the flow impingement points. Thereafter ice is completely melted at the bottom half of the windscreen and the phase change occurs gradually over the top of the windscreen which is non-physical in nature. But the melting pattern obtained from tests shows that the ice is initially melted off at the defroster flow impingement points and later the melting of ice spreads in a homogeneous way around the flow impingement points. This might be due to adopting improper material properties of ice while pre-processing the transient defroster simulation.

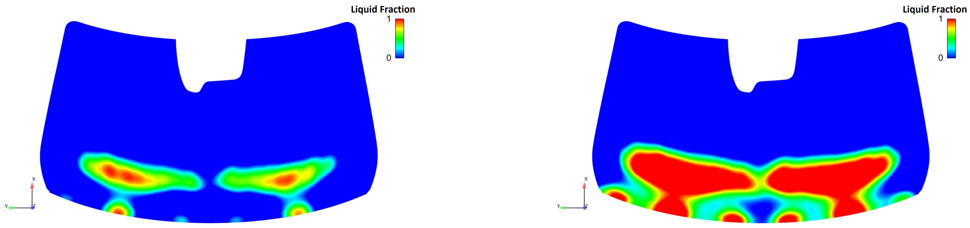

(a) (b)

Figure 4.13: *Liquid fraction β_L contour for Model with thermal air properties as constant (a) and as function of temperature (b) at the end of 900 seconds*

The accuracy of the transient defroster CFD models is also calculated for the models where thermal properties of air are modified from constant to polynomial functions of temperature. It is found that, by modifying constant air thermal properties to a temperature dependent polynomial function, the accuracy of the model D increased approximately by 23 % at the location (Location A in Figure 4.10) close the impingement point and around 21 % at the location far (Location B in Figure 4.10) from the impingement point (with respect to model A). Despite the improvement in the performance of the model D, it is better to consider the thermal properties of air as a function of temperature as it replicates the test conditions. Therefore, model D would be used to make further changes in the numerical settings of the transient model thereby advance in the accuracy of the model.

4.2.3 Influence of convective heat transfer coefficient on the melting of ice

This section provides the transient heat-up CFD simulation results and interpretations drawn when the convective heat transfer coefficient is varied over the outer boundary of ice. It is found that the nature of the profile for average temperature varies significantly when the convective HTRC varies from 0 to 17.2 w/m^2k, as seen in Figure 4.14. The temperature profile for model E is steeper than for other models and the maximum temperature approaches to 291 K. This means that the heat gained from the windscreen is not dissipated to the surroundings which leads to a significant rise in temperature inside the ice domain. Eventually it leads to the melting of ice at a faster rate relative to the rest of the transient CFD models which can be realized by plotting average liquid fraction over ice boundary(shown in figure 4.15).

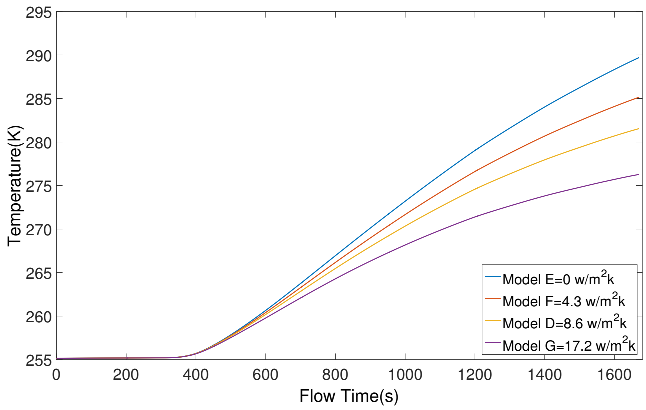

Figure 4.14: *Average temperature at the external boundary of ice*

It is to be noted that the model G has a low rise in temperature at the external boundary of ice since the heat gained from the windscreen on the other side of the ice domain is dissipated to the surroundings. This ultimately leads to the occurrence of slow phase change from ice to water. The broad range in temperature difference, between temperature profiles of model E and G seen in Figure 4.14 gives a greater possibility to correlate the melting pattern obtained from physical test results and transient heat-up simulation results.

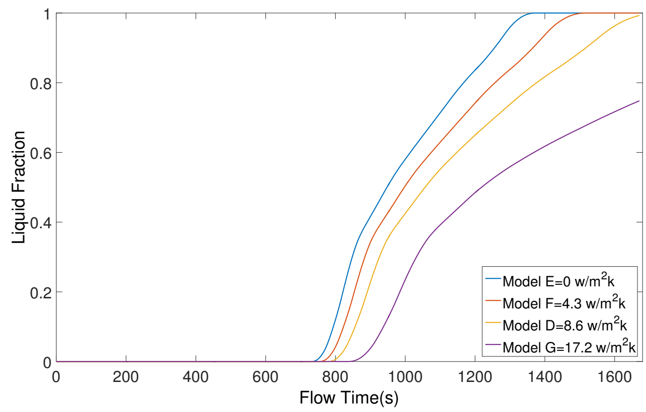

Figure 4.15: *Average liquid fraction, β_L at the external boundary of ice*

From the liquid fraction contours shown in figure 4.16, it can be validated that the melting process decreases as the convective heat transfer coefficient increases from 0 to $17.2 W/m^2k$. By comparing the liquid fraction contours it is found that the model D melting pattern matches to some extent to the test results at the end of 900 seconds. However, the melting pattern profile is different to that of physical test results after the ice is melted off around the defroster flow impingement region i.e. after 900 seconds. This can be due to the absence of gravitational and buoyancy forces as source terms in the energy equation. Moreover, the absolute density values for the ice and completely melted ice might differ from each other which leads to the retaining of heat close to defroster flow impingement regions. In addition to it the $solidification/Melting$ model does not consider the sliding of the partially melted ice over the windscreen.

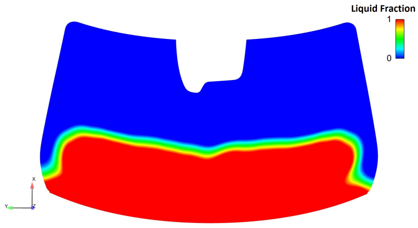

(a)

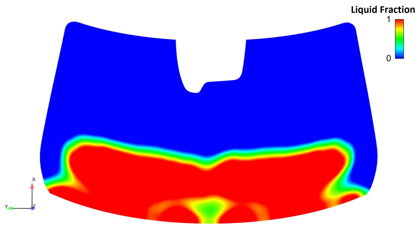

(b)

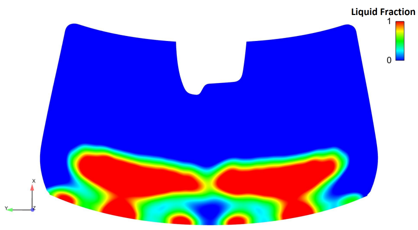

(c)

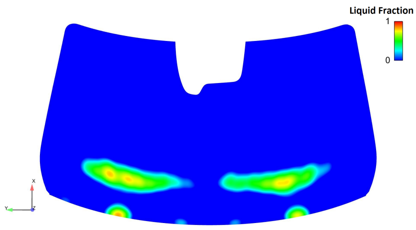

(d)

Figure 4.16: *Liquid fraction* β_L *contour for models having Convective HTRC* (W/m^2K) *of* 0 *(a),* 4.3 *(b),* 8.6 *(c) and* 17.2 *(d) at the end of 900 seconds*

The accuracy of the transient heat-up CFD models is calculated in a similar manner as mentioned in 4.2.1. By varying the convective heat transfer coefficient over the external ice boundary it was found that the accuracy of the models F and G improved approximately by 11% and 43% respectively, whereas the model E accuracy decreased approximately by 2.5 % with respect to model A at location A shown in Figure 4.10. At the location far away (Location B shown in the figure 4.10) from the flow impingement points, the accuracy of the models E, F and G increased by 29%, 78% and 89% respectively. However by correlating the melting pattern of ice between simulation model and physical test, it is concluded that the model D correlates better than model G and therefore model D is used to set-up and analyse upcoming transient heat-up models.

4.2.4 Influence of radiation on melting of ice

As the temperature of the walls mentioned in section 4.2.1 varies from $-17°C$ to $20°C$, it is interesting to know the influence of radiation on the melting of ice on the windscreen. The transient model in which the radiation model surface-to-surface is considered showed that the model did not have any significant impact with respect to the average ice boundary temperature and liquid fraction (shown in Figure 4.17 and 4.18) when compared to model D where only transient temperature profile is specified for walls.

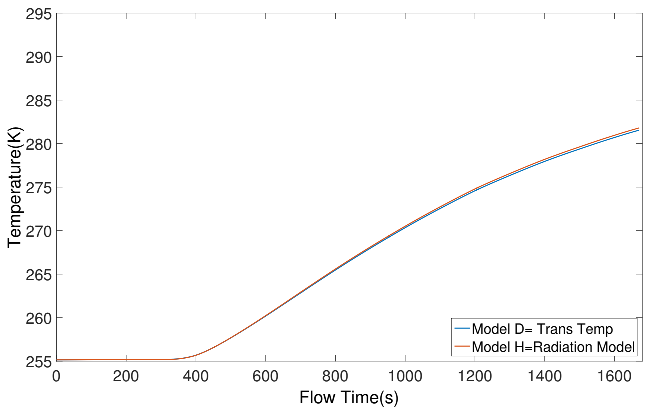

Figure 4.17: *Average temperature at the external boundary of ice*

It can be noticed that there is a insignificant influence of radiation on the average temperature of both the models. Consequently there is no change in the average liquid fraction profile of both the models as shown in Figure 4.18. By post-processing the liquid fraction contours for the models D and H it was found that the radiation did not have any effect on the melting pattern profile over the windscreen.

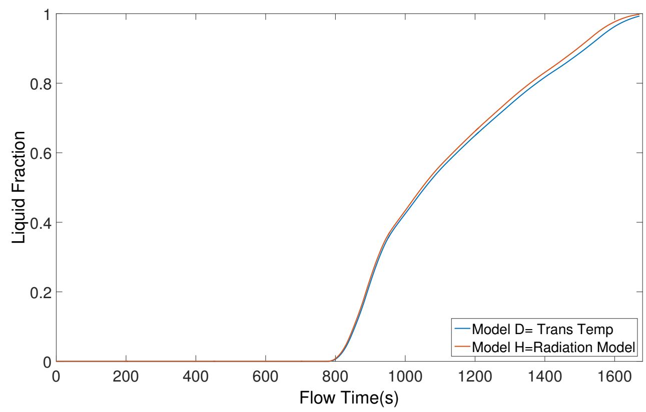

Figure 4.18: *Average liquid fraction, β_L at the external boundary of ice*

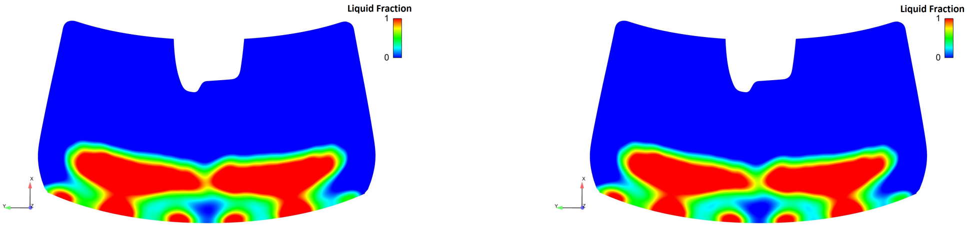

(a) (b)

Figure 4.19: *Liquid fraction β_L contour for Model with radiation (a) and without radiation (b) at the end of 900 seconds*

Finally, the accuracy of the models is calculated with respect to model A and it was found that the accuracy of the model H is 3%, which is less when compared to model D whose accuracy is approximately 23 % at the location close (Location A shown in Figure 4.10) to the flow impingement regions. However, at the location (Location B shown in Figure 4.10) far away from the flow impingement point, the accuracy of the model H increased by 45%. As the liquid fraction contours do not correlate to the physical test at the location far away from the flow impingement regions, model D is preferred over the model H to analyse the remaining transient heat-up CFD models.

4.2.5 Influence of numerical schemes on the melting of ice

As the numerical schemes are used to discretize the unsteady, advection and conduction terms in the energy equation, it would be interesting to see the influence of discretization schemes on transient heat-up simulation results. The pre-processing setup for the models I and J are similar to model D. It was found that by using the unsteady second order scheme (with and without bounded) there was a significant difference in the average temperature rise at the external ice boundary. The average temperature rise for models I and J is found to be same throughout the flow time. However, it was less when compared to model D, which is shown in Figure 4.20. It is to be noted that due to the consideration of thermal properties of air as polynomial function of temperature, there is a considerable offset in the temperature profiles of model D and other models (I and J), whereas the offset is minimal when thermal properties of air are constant throughout the flow time. Therefore proper care has to be taken while selecting the discretization scheme in solving the transport equations numerically.

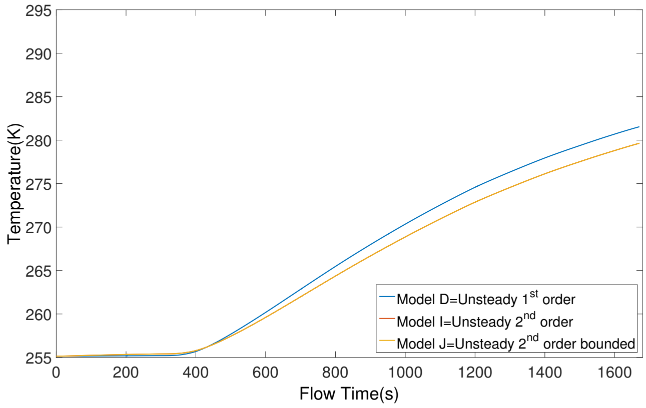

Figure 4.20: *Average temperature at the external boundary of ice*

This difference in the temperature rise between the models is reflected in the liquid fraction plot, where the melting of ice for the model D is complete. Whereas for the models I and J melting has taken place to a extent corresponding to a liquid fraction of 0.935 for the entire defroster flow time. In addition, there is a delay of 70 seconds in the melting process for the models I and J when compared to model D, which can be noticed in Figure 4.21.
This delay in the melting time to attain certain average liquid fraction lead to the different liquid fraction

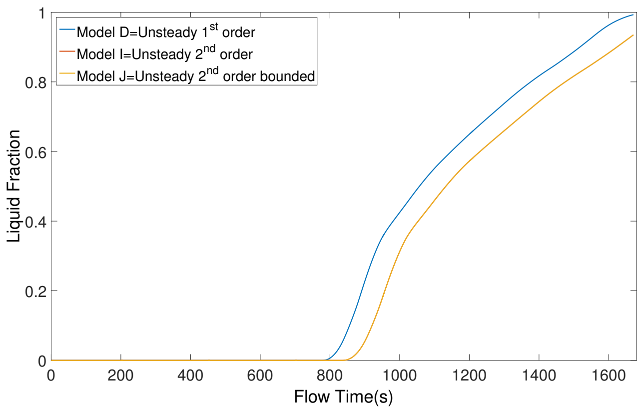

Figure 4.21: *Average liquid fraction, β_L at the external boundary of ice*

contours between the referred models. From Figure 4.22 it is realised that the amount of melting taking place in the model D is substantially high when compared to other models at the end of 900 s. By comparing melting patterns from the physical test it is clearly visible that the model D is closely related to the test results. Yet, further improvement in the model is essential to match the melting pattern of physical tests.

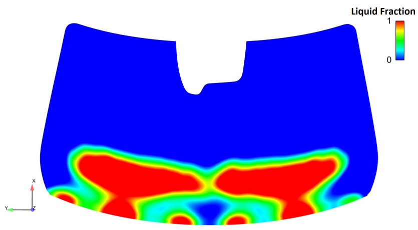

(a)

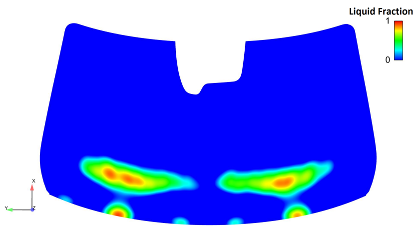

(b)

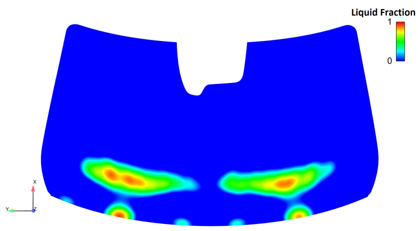

(c)

Figure 4.22: *Liquid fraction β_L contour for Model using first order unsteady scheme (a), unsteady second order (b) and unsteady second order bounded (c) scheme at the end of 900 seconds*

Although there is a major influence of numerical schemes on the transient heat-up simulation results, it would be interesting to know how accurate the models are when compared to model A. It was found that the accuracy of the models I and J is less than for the model A at coordinate (Location B shown in the figure 4.10) far away from defroster flow impingement regions. However, the accuracy of the models I and J is nearly 80% greater than model A at location close to the flow impingement region. Furthermore by comparing the liquid fraction contours for the models I and J to the physical test, it is evident that the model with the unsteady first order scheme provides better results than the other models. Since the efficiency of the model is based on accuracy and melting pattern of ice over the windscreen, it is concluded that model D works better than the other models and therefore model D is used to analyse further models.

4.2.6 Influence of heat energy supply on the melting of ice

From the physical test data it was possible to compute the heat energy supplied to the air across the heater. Moreover, the mass flow rate of air (equivalent to volume flow rate of 100 l/s) was calculated based on the heat transferred to the air through the heating medium. It is to be noted that a constant temperature of $255.15K$ was provided at the inlet of HVAC unit for the model K and mass flow rate equivalent to 100 l/s was specified as inlet mass flow rate for the model D. Having supplied heat energy across the heater, it was found from Figure 4.23 that the temperature rise was quite rapid for model K when compared to model D for at least half of the defroster time and later vice versa. This indicates that the melting of ice occurs quicker for model K at first half of the defroster flow time and later model D. When the average temperature for both the models attain approximately 273 K, model K would result in a larger melting of ice than model D which can be seen in figure 4.25. Furthermore the model K implementation is closely related to the conditions to physical tests.

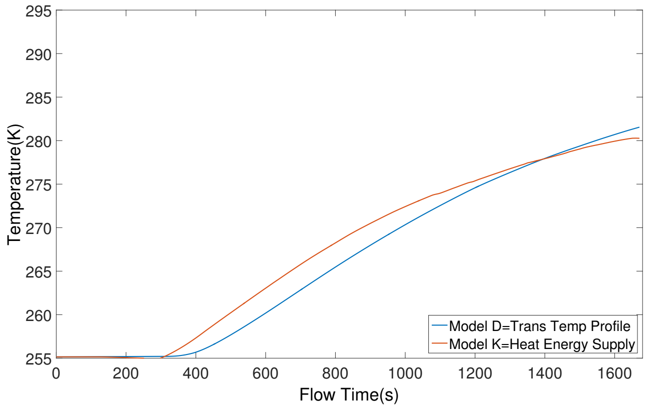

Figure 4.23: *Average temperature at the external boundary of ice*

The heat energy supplied across the heater eventually had an impact on the average liquid fraction over the external boundary of ice. From Figure 4.24 it is clear that the rapid rise in temperature during the first half of the defroster time reflected in the average liquid fraction rising to 0.6 in a shorter interval of time than the model D.

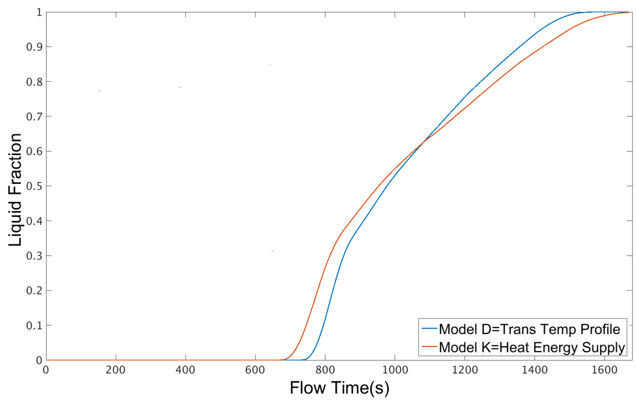

Figure 4.24: *Average liquid fraction, β_L at the external boundary of ice*

The difference in the melting of ice between the models can be observed by looking at Figure 4.25

which shows the melting pattern of ice on the windscreen at the end of 900 seconds. In this figure it can be noticed that the ice is melted more around the defroster flow impingement regions for model K when compared to model D.

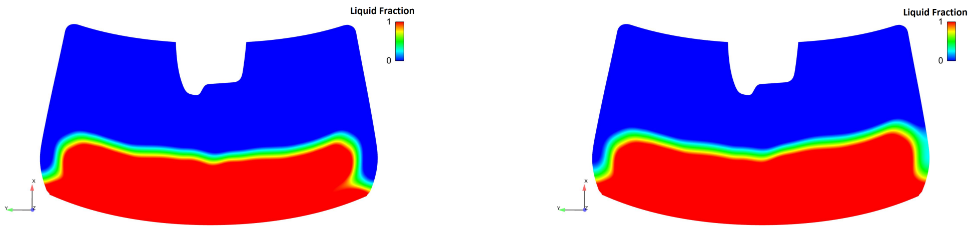

(a) (b)

Figure 4.25: *Liquid fraction β_L contour for Model using transient temperature profile (a) and supply of heat energy (b) as a thermal source*

The better correlation of model K to the physical test also reflected in the windscreen temperature that is used to calculate the accuracy of the transient CFD models. It was found that the accuracy of the model K improved by 44% when compared to model A at the location close (Location A shown in Figure 4.10) to the flow impingement region, whereas the accuracy of the model K improved by approximately 82 % than model A at the location (Location B shown in Figure 4.10) far away from the defroster flow impingement location. In addition, model D accuracy deteriorated by 19% at the coordinate near to the flow impingement region and improved by 43% at the location far away from the flow impingement region. This variation in the accuracy of the model D is due to the change in the mass flow rate specified at the inlet of the HVAC unit. The melting pattern for model D looked similar to model K at the end of 900 seconds. Henceforth it can be said that the model K correlates well to the physical test results, as there is an increase in accuracy in relation to physical test windscreen temperature and melting pattern of ice over the windscreen. By setting up various transient CFD models, it is also concluded that the use of model K led to the large improvement when compared to rest of the transient models. However, the melting of ice at the location far away from the flow impingement region does not correlate well with the liquid fraction contours obtained from tests. This also validates that the convective heat transfer coefficient has to be less than that of 8.6 w/m^2k at the location away from the flow impingement region.

It is to be noted that an attempt was made further to improve the accuracy of the model K in order to compensate the heat loss which occur at the HVAC and defroster duct walls. This can be confirmed from the defroster outlet temperature profile shown in Figure 4.26 that there is a significant offset between the temperature profile between model K and the physical test when compared to offset between temperature profile for model D and physical tests which has to be eliminated to improve the performance of the CFD models.

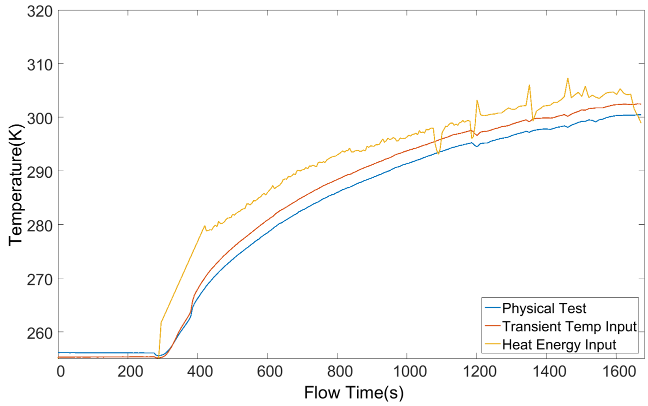

Figure 4.26: *Defroster outlet temperature profiles of model K, model D and physical test*

The heat loss at the HVAC and defroster ducts and the consumption of heat to warm the components in the ducts are considered by increasing the convective heat transfer coefficient at the external boundary of ice to 17.2 w/m^2k. An attempt was made to remove the heat in the domain by increasing the heat transfer coefficient at the external boundary of ice. It was found that the accuracy of the model improved by 21 % than model K near the flow impingement region however the accuracy of the model decreased by 22% at the location far away from the flow impingement region but the liquid fraction contour at the end of 900 seconds had a poor correlation when compared to test. Therefore, it cannot be stated that the transient model having convective heat transfer coefficient of 17.2 w/m^2k can be used to overcome the heat loss at the duct walls. Proper care has to be taken to reduce the defroster outlet temperature thereby the correlation of internal windscreen temperature improve with respect to the physical test.

5 Physical Test Results

A defroster test is conducted at the Volvo Cars climatic cold chamber. The defroster testing is carried out as per SAE J902A passenger car windscreen deicing test procedure. Volvo V40 with a petrol engine is used for performing the defroster test.

Defroster tests are carried out with and without using windshield wipers. However the test data obtained from the tests without using wipers are used for specifying the transient temperature profiles at the walls close to windscreen and the amount of heat energy gained by air across the heater to perform simulations. Later, the test results are used to validate the simulation results. The results for the test conducted without wipers are used because the wipers used to wipe the partially melted ice on the windscreen also acted like a scrubber which led to the removal of ice over the windscreen. It is to be noted that the melting patterns are recorded at the end of 5, 10, 15, 20, 25 and 30 minutes during the tests. Figure 5.1 shows the melting pattern of ice over the windscreen at various intervals of time for two defroster tests conducted without using wipers. The melting contours are recorded by a passenger sitting inside a car. The values in Figure represent the time (minutes) and the contours are drawn using black and red sketches which represents the two tests conducted without using wipers. It can be seen from Figure 5.1 that as the duration of test time is increasing the melting area increasing from the defroster flow impingement points to far away from these regions. This eventually leads to the melting of ice throughout the windscreen. However there is a small amount of ice on both the sides of the windscreen as well as at the bottom of the windscreen does not melt during the test.

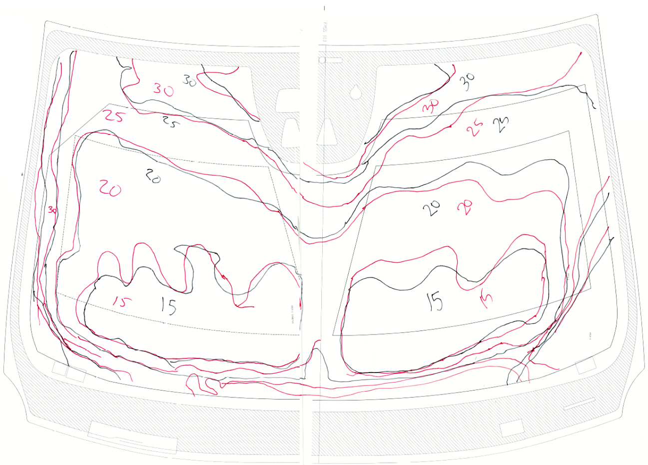

Figure 5.1: *Ice melting pattern at various intervals of time during physical test*

5.1 Correlation of Simulation Results to Physical Test Results

This section presents the information in regard to how well the simulation results correlated to the physical test results and the possible solution for further improvement in the simulation results.

From Figure 5.2 it is evident that the melting pattern at the end of 1200 seconds obtained from the simulation does not match exactly with the physical test results hown in Figure 5.3. It can also be seen in Figure 5.3 that the ice exists on the sides of the windscreen during the test but those regions are completely melted in the simulated flow. However, before the partially melted ice slides on the windscreen (not until 900 seconds) it is possible to correlate the melting pattern of ice since the latter is melted around the defroster flow impingement regions only to some extent. It is to be mentioned that the implementation of solidification and melting model did not include gravitational and buoyancy force source terms which

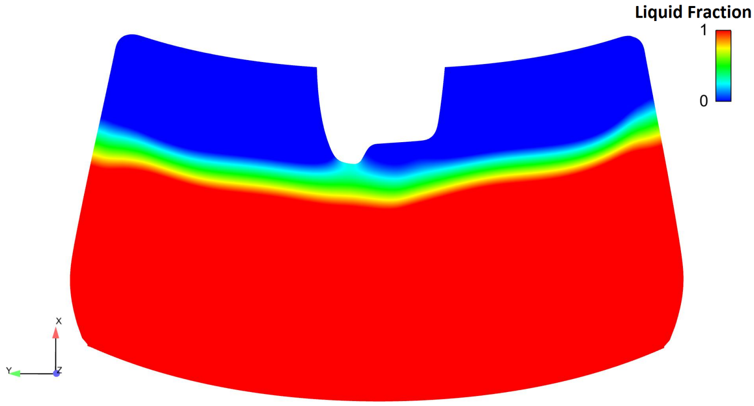

Figure 5.2: *Liquid fraction β_L contour of Model K at the end of 20 minutes*

Figure 5.3: *Liquid fraction β_L contour from the physical test at the end of 20 minutes*

leads to the lack of proper correlation. There is also a possibility that the default settings used while selecting the solidification and melting model can be altered for further improvement in the simulation results. A_{mush} parameter which refers to mushy zone constant is set to 10^5 but it can vary from 10^4 to 10^7. Therefore it is concluded that the consideration of source terms and sliding of ice in addition to an appropriate selection of A_{mush} are essential to obtain a better correlation of simulation results with respect to the physical test results. The correlation could also be improvised by removing the cells from the defroster domain when the liquid fraction reaches 1 so that the ice converted to water does not retain the heat at the defroster flow impingement region and prevent spreading of heat to the lateral sides of the windscreen. This might also eventually lead to melting of ice in a homogeneous way from the flow impingement region.

6 Conclusion

This chapter presents the results obtained while analysing steady state flow and transient heat-up analysis. In order to improve the accuracy of the windscreen deicing, it is better to use the *Realizable* $k-\epsilon$ turbulence model than the $k-\omega$ SST turbulence model while solving the defroster flow equations since $k-\omega$ SST model requires stringent requirement of $y^+ < 5$ throughout the domain and larger number of iterations to obtain convergent solutions. Furthermore, unphysical flow behaviour is observed when the flow attaches to the windscreen.

Having simulated the defroster flow, various transient CFD models were analysed in order to improve the correlation of simulation results to the physical test results. It was realised that by changing the boundary conditions from adiabatic (model A) to transient temperature thermal condition (model C) at certain walls like A-pillar, IP and front doors had a minor influence on the melting of ice. However, it is better to specify transient temperature thermal boundary condition at these walls which represents the test conditions. By changing the boundary conditions at the mentioned walls, the accuracy of the CFD model improved by 7% and 18% at the location close to and far away from the defroster flow impingement region when compared to model A.

It was found that by changing the nature of thermal properties of air from constant to a polynomial function of temperature, there was a small improvement in the performance of the transient heat-up CFD model. The accuracy of the CFD model (model D) improved by 23% and 21% at the regions close to and far away from the defroster flow impingement region when compared to model A.

Since the temperature of the air in the computational domain varied in the range of -18 to $40°C$, radiation effects at these walls did not have any influence on the performance of the transient models. This eventually led to the selection of model D over model H in which the radiation model was used along with the solidification and melting model.

It was also interpreted that the choice of discretization schemes had a certain impact on the performance of the models. It was found that that by using an unsteady first order scheme (model D) provided a solution better than the model using unsteady second order (model I) and unsteady second order bounded scheme (model J) since there was a correlation of windscreen temperature to some extent at the location near and far away from the impingement points. Between these models, model D was chosen over the other models to further improve the accuracy of the CFD models.

When the convective heat transfer coefficient was varied over the external boundary of ice, it was evident that there was a significant influence on the average temperature of ice and liquid fraction profile. The CFD model D having a convective heat transfer coefficient of 8.6 W/m^2K was chosen over the other models having different convective heat transfer coefficient since the model D melting contour was able to correlate to the physical test contour at the end of 15 minutes to some extent. The correlation of the melting pattern of ice can be further improved by fine tuning the convective heat transfer coefficient between 4.3 W/m^2K and 17.2 W/m^2K.

With the specification of heat energy source across the heater, it was possible to implement the actual physics of the flow in the HVAC unit which eventually led to a maximum increase in accuracy of 44% and 82% at the location close to and far away from the defroster flow impingement regions respectively. The large improvement in the accuracy of the model K shows the importance of heat-up curve to perform defroster heat-up simulation. In order to further improve the accuracy of the CFD model (model K), the heat loss in HVAC and defroster units has to be taken into account which can be achieved by reducing the fraction of heat supplied to air across the heater. Moreover, the influence due to gravitational force, buoyancy force and sliding of ice over the windscreen has to implemented to obtain higher accuracy of CFD models.

7 Future Work

This chapter presents possible future work to improvise accuracy of transient CFD models to a further extent. With the amount of understanding obtained while executing this master thesis it is believed that, by taking in to consideration the effect of gravitational force and buoyancy force in the energy equation, the melting pattern obtained at the external boundary of ice could be correlated well to the physical test. In addition, it would be interesting if the solver has a capability to consider the sliding of ice while performing transient heat-up simulation. Moreover, the heat loss at the HVAC and defroster duct walls has to be measured and incorporated while performing transient heat-up simulations. Although the windscreen temperature correlated well at the top of the windscreen while varying convective heat transfer coefficient at the external boundary of ice, there was still a lack of correlation of melting pattern to the physical test throughout the defroster flow time. Therefore, it would be better to assign a varying convective heat transfer coefficient over the windscreen area for further improvement of transient heat-up model performance. In addition, it would also be better to remove the cells at the external boundary of ice when the liquid fraction reaches one so that the melting of ice occurs in a homogeneous way. Last but not least it would be better to measure the thickness of ice during the physical test as the correlation of melting ice pattern is used to measure the performance of the defroster CFD models.

References

[1] L. Davidson. *Fluid mechanics, turbulent flow and turbulence modeling*. 2016.

[2] H. Versteeg and W. Malalasekera. *An Introduction to Computational Fluid Dynamics,The Finite Volume Method*. 1995.

[3] M. Saukkonen. Transient Simulation of Windscreen Deicing. *Examensarbete/Chalmers tekniska högskola* (2002).

[4] T.-H. Shih et al. A new $k-\epsilon$ Eddy-Viscosity Model for High Reynolds Number Turbulent Flows - Model Development and Validation. *Computers Fluids* (1995).

[5] *ANSYS Fluent Theory Guide*. Ansys inc. Canonsburg, United States of America, 2013. URL: https://uiuc-cse.github.io/me498cm-fa15/lessons/fluent/refs/ANSYS%20Fluent%20Theory%20Guide.pdf.

[6] S. Kim et al. A Computations of Complex Turbulent Flows Using the Commercial Code ANSYS Fluent. *In Proceedings of the ICASE/LaRC/AFOSR Symposium on Modeling Complex Turbulent Flows* (1997).

[7] F. Menter. Review of the SST Turbulence Model from an Industry Perspective. *International Journal of Computational Fluid Dynamics* (1994).

[8] V. Roller. Modelling Solidification Process (1987).

[9] V. Roller and C. Prakash. A Fixed-Grid Numerical Modeling Methodology for Convection-Diffusion Mushy Region Phase-Change Problems. *International Journal of Heat Mass Transfer* **30**.8 (1987), 1709–1719.

[10] B. Thomas et al. Fixed grid techniques for phase change problems: A Review. *International Journal for Numerical Methods in Engineering* **30** (1990).

[11] SAE J902A: Passenger Car Windshield Defrosting Systems (1967).